Journal of Medicinal Chemistry

pubs.acs.org/jmc

Article

Discovery, Optimization, and Preclinical Pharmacology of EP652, a METTL3 Inhibitor with Efficacy in Liquid and Solid Tumor Models

Guillaume Dutheuil,* Killian Oukoloff, Julien Korac, François Lenoir, Mohamed El Bousmaqui, Nicolas Probst, Alexey Lapin, Galina Nakhabina, Catherine Sorlet, Nicolas Parmentier, Delphine Karila, Nugzar Ghavtadze, Paméla Casault, Stephen Claridge, Selma Sapmaz, Martin J. Slater, and Graeme L. Fraser

Cite This: *J. Med. Chem.* 2025, 68, 2981−3003

Read Online

ACCESS | Metrics & More | Article Recommendations | Supporting Information

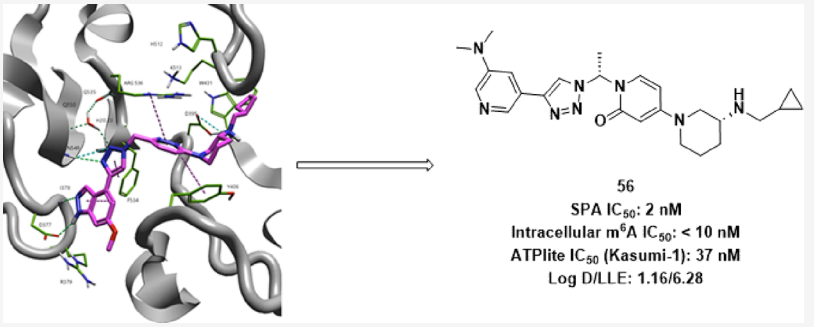

ABSTRACT: METTL3 is the RNA methyltransferase predominantly responsible for the addition of N^6-methyladenosine (m^6A), the most abundant modification to mRNA. The prevalence of m^6A and the activity and expression of METTL3 have been linked to the appearance and progression of acute myeloid leukemia (AML), thereby making METTL3 an attractive target for cancer therapeutics. We report herein the discovery and optimization of small-molecule inhibitors of METTL3, culminating in the selection of **EP652** as an *in vivo* proof-of-concept compound. **EP652** potently inhibits the enzymatic activity of METTL3, has favorable PK parameters, and demonstrates efficacy in preclinical oncology models, indicating that pharmacological inhibition of METTL3 is a viable strategy for the treatment of liquid and solid tumors.

INTRODUCTION

N^6-Methyladenosine (m^6A) is the most abundant internal chemical modification of eukaryotic mRNAs[1] and affects the fate of its target transcripts in terms of splicing, transport, stability, or translation ratio.[2] The modification is catalyzed by a methyltransferase complex, for which methyltransferase-like 3 (METTL3) constitutes the catalytically active "writer" enzyme,[3] while methyltransferase-like 14 (METTL14) is essential to stabilizing the complex and permits the formation of the binding pocket. The METTL3−METTL14 complex[4] transfers a methyl group from *S*-adenosylmethionine (SAM) to the adenosine. The majority of m^6A modifications in mRNA are found within a five-residue sequence, with an invariant adenosine and with cytosine and nucleotide variations occurring at the −2, − 1, and +2 positions, most commonly 5′-(A/G/U)(G/A)AC (A/C/U)-3′. This sequence pattern is termed the DRACH motif, and modification of the central adenine base (bolded in the above sequence) to m^6A is catalyzed by the methyltransferase enzyme complex METTL3/METTL14. To date, all known inhibitors have been shown to interact at the SAM binding pocket of METTL3 and are therefore referred to as METTL3 inhibitors.

METTL3 is a druggable target in the field of RNA epitranscriptomics with application in the treatment of cancer. Thus, heightened METTL3 expression and/or increased prevalence of its output marker, m^6A, is inversely correlated with survival in various liquid and solid tumors.[5] Numerous reports indicate that METTL3 alters the synthesis of various oncoproteins and pro-apoptotic proteins to modulate tumor progression.[6] These data have spurred interest in METTL3 as a cancer target with a novel mechanism of action. At the outset of this project, no selective inhibitor was available, and the only known reference compound was the universal nucleoside analogue sinefungin, which inhibits most methyltransferases

Received: September 18, 2024
Revised: December 19, 2024
Accepted: January 17, 2025
Published: January 30, 2025

https://doi.org/10.1021/acs.jmedchem.4c02225
J. Med. Chem. 2025, 68, 2981−3003

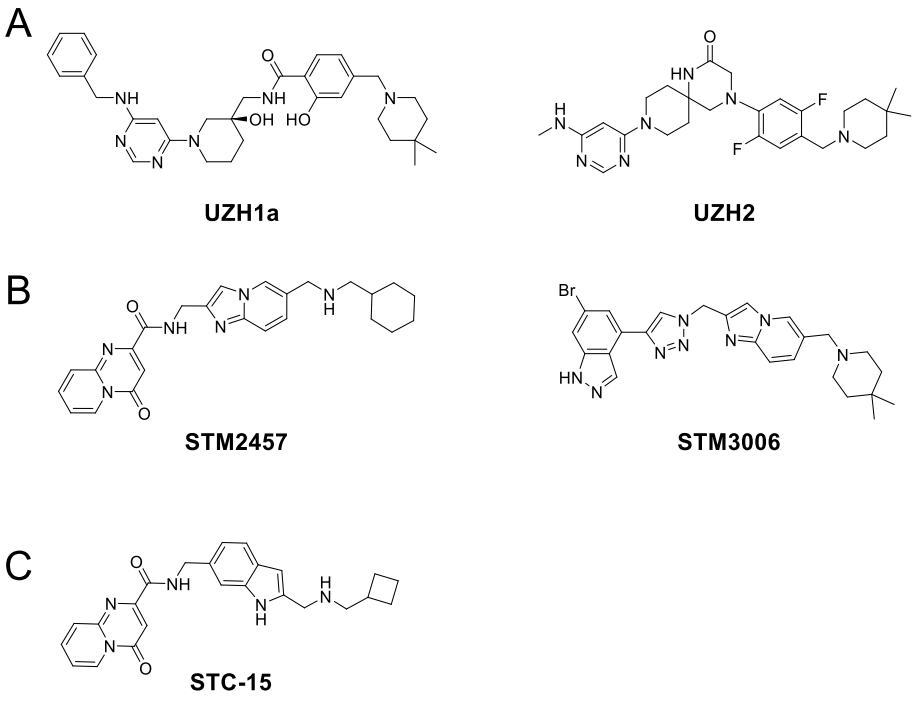

Figure 1. Small-molecule METTL3/14 inhibitors reported in literature: (A) are from Caflisch's group at University of Zurich, (B) are Storm's published compounds, (C) is Storm's clinical candidate STC-15.

and is not selective for METTL3.[7] Following the publication of the first (non-nucleoside) inhibitors developed against METTL3, namely, UZH1a (Figure 1A) by the Caflisch group[8] at Zurich University and STM2457 (Figure 1B) by Storm Therapeutics,[9] additional synthetic inhibitors have since been reported principally led by these two organizations.[10] Thus, the Caflisch group has now published a SAM-based series,[11] an improved UZH1a scaffold,[12] and developed an advanced bridged series (UZH2, Figure 1A),[13] while Storm Therapeutics has published compounds with superior potency to STM2457, namely, STM3006 (Figure 1B),[14] and deposited several patents[15] disclosing the first-in-class METTL3 inhibitor STC-15 (Figure 1C), a compound that has advanced into first-in-human studies.[16] Accent Therapeutics has published three patents on their METTL3 program derived from SAM-like nucleoside structures,[17] and 858 Therapeutics has recently published[18] their METTL3 inhibitors, which present a similar chemotype to STM2457. To date, only STC-15 has been proven to have an appropriate profile for advancement into clinical development.

In this article, we describe the use of QSAR modeling in the discovery of a series of METTL3 inhibitors based on hit **1**. Through a multiparameter optimization process, we were able to discover compound **56**, which was selected as our proof-of-concept compound (**EP652**). Herein, we disclose the pharmacological, ADME, and pharmacokinetic profile of compound **56** in addition to *in vivo* efficacy in AML as well as solid tumor models.

RESULTS AND DISCUSSION

Discovery of Hit Compound 1. At the outset of the project, parallel activities including high-throughput screening (HTS, both by MTase-Glo and Affinity Selection-Mass Spectrometry (ASMS)[19] assays), virtual screening, and ligand-based drug design (LBDD) were deployed to identify chemical starting points. Briefly, the HTS and virtual screening[20] approaches did not yield chemical matter that survived hit expansion due to low hit rates in primary screening, relatively high incidences of nonspecific ligand affinity and assay interference. Meanwhile, the LBDD approach was bolstered by crystallographic evidence for small-molecule inhibitors (UZH1a (pdb: 7ACD) and STM2457-like (pdb: 7O2I) structures; see Figure 1) bound to the truncated METTL3/14 complex, allowing the use of structure-based drug design (SBDD) to complement the ligand-based approach. We hypothesized that these chemotypes converged at the exploitation of at least two binding elements in this enzyme. Our modeling[21] of these systems (Figure 2, top) indicated that the small-molecule inhibitors interact with the recognition sites in both the adenosine part of the SAM binding domain and in the RNA substrate recognition site in a manner consistent with the observed structure−activity relationships. This hypothesis has since been supported by the release of confirmatory X-ray data (pdb: 7O2I).[8,9,14] This understanding of the ligand−enzyme interaction refined our approach to look for alternate scaffolds by docking. Indeed, field analysis of UZH1a and Storm compound 270 (patent numbering, OMe variant of STM3006, Figure 2, top) revealed an obvious overlap between both reference compounds and a clear distribution of positive and negative fields in dedicated regions.

Extended analysis of key subseries from the Storm patent,[15] namely, the triazole-indazoles (such as STM3006) and amide-pyridopyrimidones (such as STM2457), docked into our model (Figure 2 Bottom) led us to conclude that the core units of those structures were mostly aromatic spacers (with an additional pi-stacking and cation−pi contribution) between two rotulas on each side, allowing proper interactions of the aromatic head groups on one side (Figure 2) and of the amino-alkyl groups on the other side. Moreover, we concluded that both the triazolo-indazole and amide-pyridopyrimidone fragments should similarly be interpreted as unified moieties

https://doi.org/10.1021/acs.jmedchem.4c02225
J. Med. Chem. 2025, 68, 2981−3003

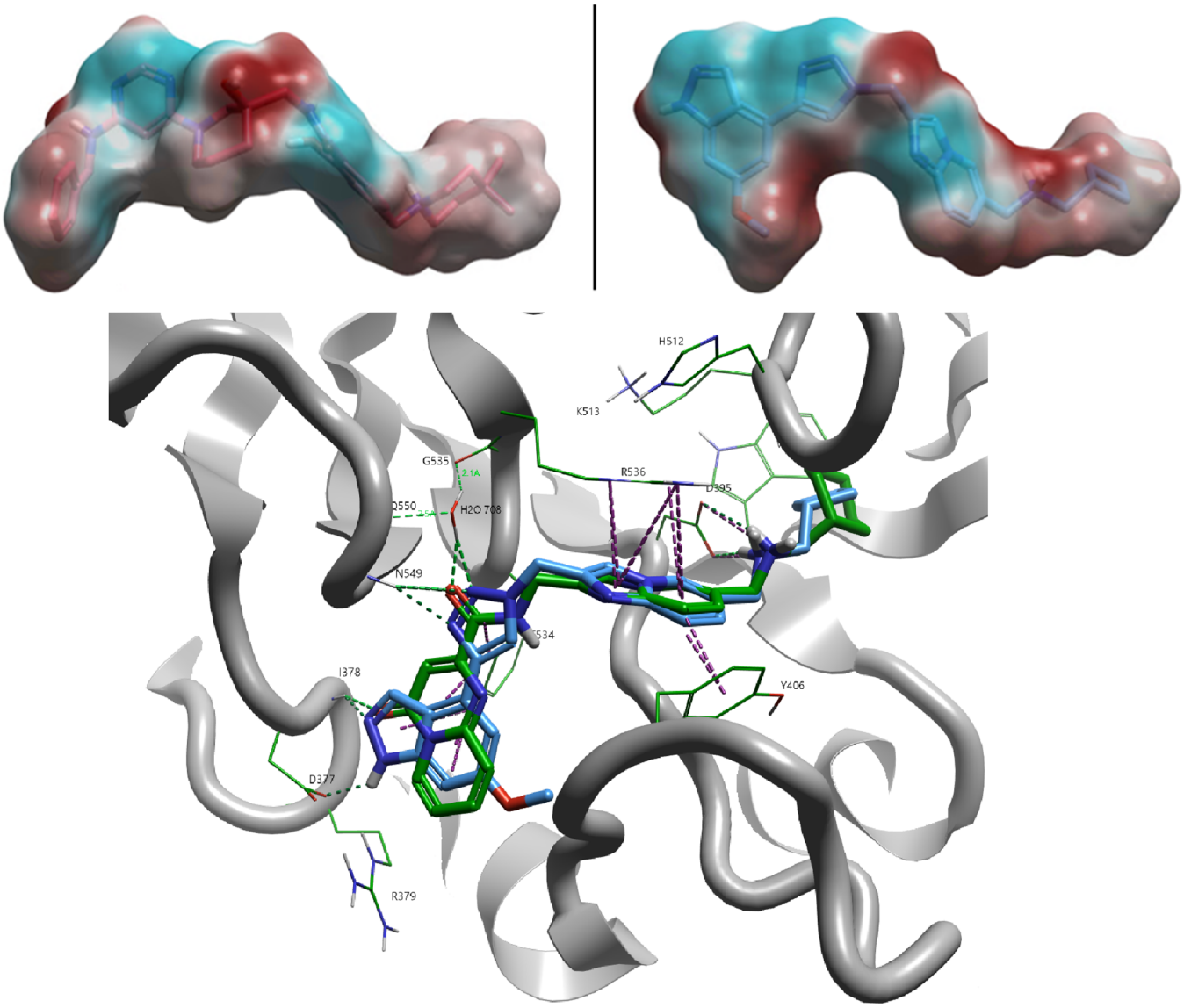

Figure 2. Top: comparison of electrostatic surface of **UZH1a** (left) and **Storm#270** (right) from the X-ray data (negative field in blue, and positive field in red) are represented. Bottom: substructure alignments of **Storm#270** (blue) with **STM2457** (from PDB:7O2I— green structure). Hydrogen bonds and cation−pi and pi stacking interactions are highlighted as dashed lines.

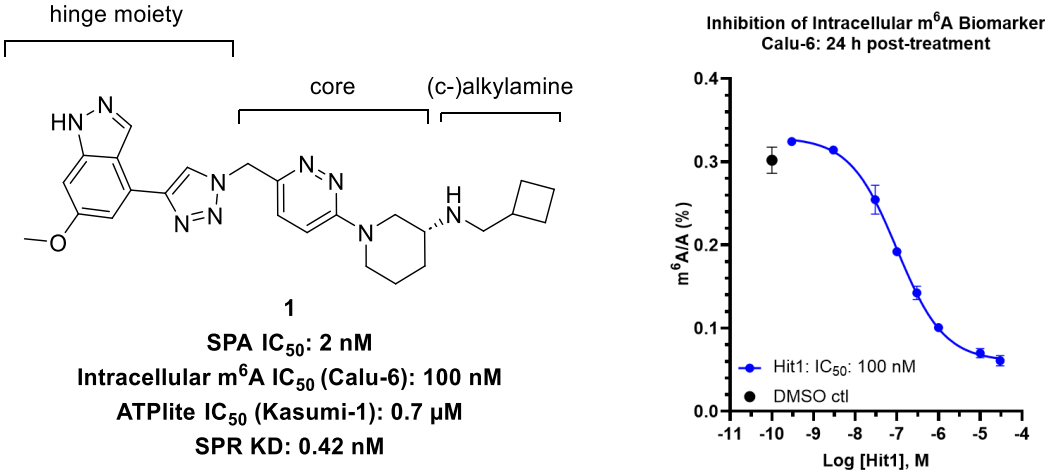

Figure 3. Initial compound **1** hit was obtained by *in silico* core replacement and representative inhibitory data, highlighting m^{6}A cellular quantification by LC-MS/MS in mRNA from Calu-6 cells after 24 h treatment with **1**.

https://doi.org/10.1021/acs.jmedchem.4c02225
J. Med. Chem. 2025, 68, 2981−3003

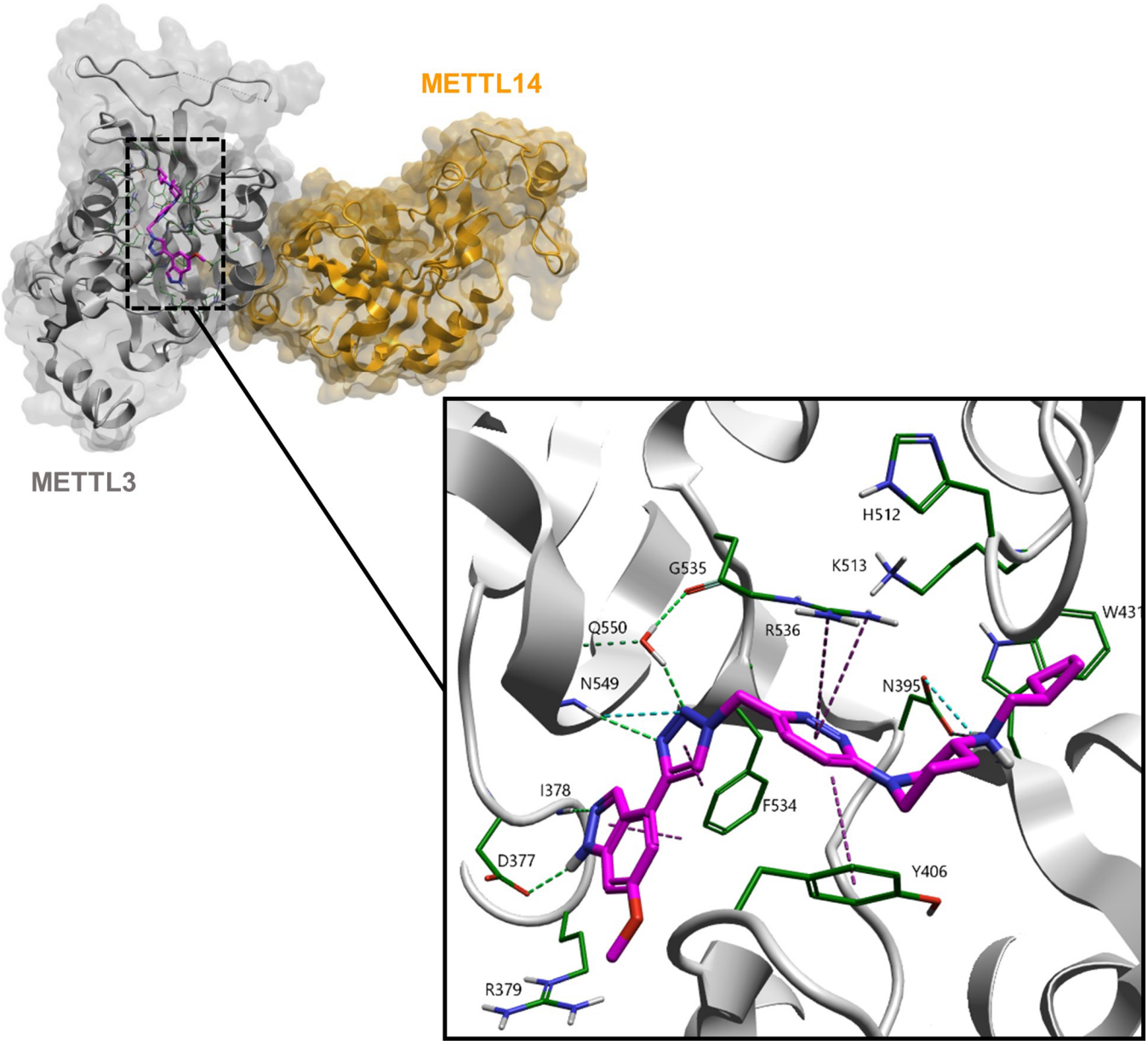

Figure 4. Cartoon representation of the entire crystal asymmetric unit of truncated METTL3:METTL14 in complex with compound **1**. The structure of METTL3 is shown in gray, METTL14 is shown in orange, bound compound **1** is shown as magenta sticks. The structure of compound **1** and its binding to METTL3 is zoomed. Residues presented as green sticks are located within 4 Å of the compound. The dashed lines represent interactions (H-bonds and cation−pi and pi stacking).

("hinge"), as a whole, rather than individual functions and aromatics (Figure 3).

Based on those hypotheses and findings, we were able to develop a QSAR model and thereby pursued *in silico* core replacement with the aim of identifying novel scaffolds with physiochemical properties predicted to impart an improved ADME/PK profile.[22] The full description of our modeling approach and the workflow used are detailed in the Supporting Information. This scaffold hopping exercise was performed using Cresset's proprietary fragment replacement tool, Spark.[23] Careful selection criteria for the output ideas, including docking[24] and electrostatic complementarity (EC),[25] allowed prediction for target affinity whereas physiochemical property criteria (e.g., MW, LogP, TPSA, and flexibility) as well as synthetic feasibility assessment were additionally used to prioritize the synthesis of eight concept molecules, one of which was chemical hit **1** (Figure 3, most potent design).

This preferred hit **1** (Figure 3) was extremely potent in our SPA primary assay. The inhibition of METTL3/14 by **1** was confirmed in an orthogonal assay by measuring concentration-dependent inhibition of m^6A on mRNA samples collected from several cell lines *in vitro* (for example, results in Calu-6 are shown in Figure 3 with consistent results also determined in A549, SK-OV-3, FaDu, and Kasumi-1). Compound **1** also demonstrated antiproliferative effects: the latter was measured in cell viability assays (ATPlite) following a 72 h treatment of various cell lines (MOLM-13, Calu-6, Caov-3, KG1a, A549, SK-OV-3, FaDu, Kasumi-1, MV-4−11), confirming efficient inhibition of cancer proliferation in cellulo.

We further validated and characterized the binding of our lead compound to METTL3/14 complex by X-ray crystallog-

https://doi.org/10.1021/acs.jmedchem.4c02225
J. Med. Chem. 2025, 68, 2981−3003

raphy (at 2.1 Å resolution), confirming the binding of compound **1** at the SAM binding site (Figure 4), as anticipated.[26]

Our acquired cocrystal with **1** showed that the active binding site was very well superimposed with recently published data by Caflish's group (7O2F with UZH2) and Storm Therapeutics (7O2I with STM2457) to thereby refine our accurate determination and positioning of constituent loop structures.

Hit to Lead SAR. Optimization of hit compound **1** was monitored by routine testing in SPA as a primary assay followed by assessment of cell viability assay using ATPlite in various AML[6,27] cell lines (e.g., Kasumi-1 and MV-4−11). An initial emphasis was placed on lipophilic ligand efficiency (LLE)[28] as a predictive marker of improved safety profiles where LLE was calculated using pIC_{50} values determined by ATPlite in Kasumi-1 cells. We decided to use pIC_{50} based on the cellular assay for LLE calculation, instead of an assay directly measuring enzymatic inhibition (for example, SPA, even though such data are reported herein) due to the limited dynamic range of the enzymatic inhibition assay to distinguish between highly potent compounds (e.g., compounds with IC_{50} < 3 nM in SPA). In comparison to SPA, the ATPlite assay measuring cell proliferation proved to be a superior assay to distinguish between potent compounds and, furthermore, incorporates any differences in cellular penetration relating to the intracellular targeting required for METTL3 inhibition. Even though **1** is very potent in SPA and ATPlite assay on Kasumi-1 (Figure 3), it has poor predicted profile for drug development with strong CYP3A4 inhibition (IC_{50} ∼ 0.8 μM), poor rat liver microsome half-life (16 min) and suboptimal unbound[29] PK parameters (oral AUC unbound 1.3 μM.min, with unbound Cl of 1581 mL/min/kg).

We explored SAR beginning with the 3-aminopiperidine moiety. After a quick confirmation that the absolute configuration on the 3-aminopiperidine was crucial to potency (as deduced from modeling; see **2** in Table 1), we further confirmed that 3-amino basicity was indispensable for potency, as exemplified by the poor potency of amide analogue **3**. Methylated hit compound analogue **4** highlighted the importance of the NH interaction with Asp395 (Figure 4).

With an objective to avoid adding lipophilicity unless justified by an important improvement in potency, we systematically assessed various alkyls (compounds **5** to **11** as representatives, Table 1). Small alkyl groups were required for affinity (**5** poorly potent), whereas incorporation of larger cycloalkyl groups (**6** versus **7**) only increased LogD without concomitant increases in potency according to the Kasumi-1 ATPlite assay. Additional substitutions proximal next to the nitrogen atom (**1** versus **6**, **7**, **9**, or **10**) seemed to be detrimental for permeability, as demonstrated by decreased IC_{50} in the ATPlite assay. Interestingly, CH_2-*c*Pr (**11**) presented an alternative to the CH_2-*c*Bu of **1** although detrimental to potency (identical LLEs, and RLM $T_{1/2}$ of 17 min identical to **1**). We confirmed that CH_2-*c*Bu of **1** was the best template for us, moving forward as we shifted to SAR exploration of other moieties.

We explored chemical variations around the piperidine moiety and confirmed that it was a crucial structural element through the chair conformation, allowing proper positioning of the 3-amino moiety (Figure 4). Indeed, pyrrolidine **12** and 4-amino-piperidine **13** were poorly potent in our ATPlite assays.

Table 1. SAR around 3-Aminoalkyl Moiety of 1

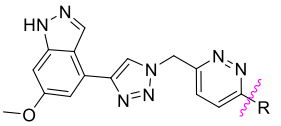

Cpd	R	SPA IC_{50} (nM)	Kasumi-1 IC_{50} (nM)	Log $D_{7.4}$	LLE[a]
1	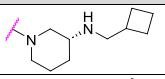	2	629	1.89	4.34
2	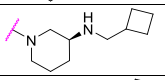	24	3405	1.89	3.56
3	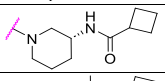	2498	> 30000	2.61	< 1.91
4	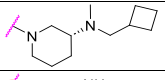	6	3128	2.59	2.91
5	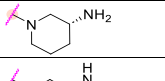	243	> 30000	1.01	< 3.52
6	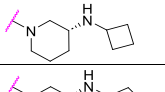	5	2743	1.71	3.85
7	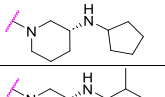	4	3428	1.88	3.59
8	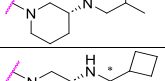	3	1757	1.92	3.84
9*	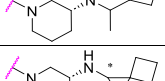	2	10126	2.14	3.34
10*	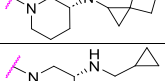	4	1103	3.06	2.90
11	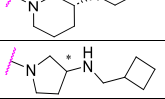	2	1054	1.63	4.35
12*	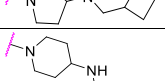	235	15251	1.95	2.87
13	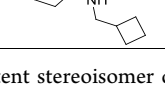	563	> 30000	1.64	< 2.89

*Most potent stereoisomer data provided. [a]LLE = pIC_{50} (Kasumi-1) − LogD.

We continued our SAR exploration of this piperidine region, after having implemented first the simplification of our hinge moiety, by replacing the lipophilic indazole of **1** by a pyridine such as 3-methoxypyridine in **14** (Table 2). The latter change (more SAR shared below) allowed us to maintain LLE as the decrease in potency was compensated by the decrease in lipophilicity (**14** versus **1**). This structural change provided a better template in terms of ADME profile (improved RLM ($T_{1/2}$ now 112 min) and PPB, slightly ameliorated CYP profile versus **1**). We then continued our SAR exploration by modifying further the piperidine moiety toward azepane (**15**) and spiro aminocycles (exemplified with **16** and **17**). None of the modifications attempted led to any interesting inhibition, highlighting again the ideal conformation obtained with the 3-aminopiperidine as predicted from our QSAR model. The 3-aminocyclohexyl **18** also presented poor inhibition as expected from the considerable conformational change between axial positioning of pyridazine with cyclohexane against quasi-planar pyridazine positioning with piperidine.[30] Similarly, 3-amino-piperidone **19** exhibited poor inhibition consistent with its potential clash with carboxylic acid from Asp395. Finally,

https://doi.org/10.1021/acs.jmedchem.4c02225
J. Med. Chem. 2025, 68, 2981−3003

Table 2. SAR around the Piperidine Moiety

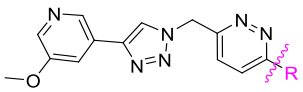

Cpd	R	SPA IC_{50} (nM)	Kasumi-1 IC_{50} (nM)	Log $D_{7.4}$	LLE[a]
14	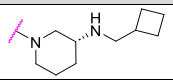	6	1931	1.47	4.24
15*	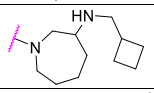	50	> 30000	1.18	< 3.35
16	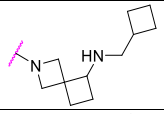	2299	> 30000	1.54	< 2.99
17*	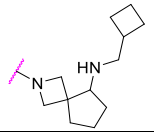	205	> 30000	1.85	< 2.68
18*	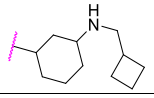	215	> 30000	1.55	< 2.98
19	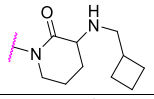	> 30000	> 30000	1.15	< 3.38
20	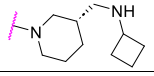	124	> 30000	0.88	< 3.65

*Most potent stereoisomer data provided. [a]LLE = pIC_{50} (Kasumi-1) − LogD.

Table 3. SAR around Core of 16

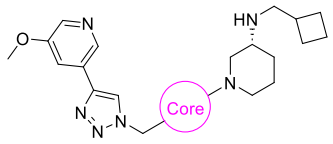

Cpd	Core (hetero)cycle	SPA IC_{50} (nM)	Kasumi-1 IC_{50} (nM)	Log $D_{7.4}$	LLE[a]
21	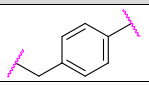	6	875	2.04	4.02
22	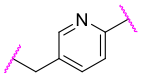	7	1202	1.46	4.46
23	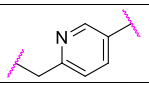	4	894	1.21	4.84
24	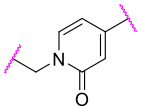	3	1104	1.51	4.45
25	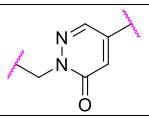	26	11814	1.06	3.87

[a]LLE = pIC_{50} (Kasumi-1) − LogD.

shifting the nitrogen position toward *c*Bu (**14** toward **20**) led to an order of magnitude decrease in potency as one could expect based on the importance of the interaction between Asp395 and the amino group (Figure 4). Substituted piperidines (not shown) were made, as well, without any potency improvement. This avenue was discontinued in light of the increased complexity (chiral centers) and building block cost or synthetic access.

We then turned our attention toward core modification of our hit compound **14**. Several interesting cores allowed us to make potent compounds while affording a variety of structural features (Table 3). Potencies in SPA and ATPlite (Kasumi-1) were typically in the same range with most six-membered aromatics such as compounds **21** (phenyl core), **22** (2-pyridine core), **23** (3-pyridine core), and **24** (pyridone core). Those results confirmed our observation that the core region may be considered as a spacer mostly between "hinge" and aminoalkyl moieties. However, we obtained poorly potent compounds for other synthesized six-membered aromatics derivatives bearing 2-nitrogens such as pyridazinone **25** (clash between extra nitrogen and carbonyl backbone of Phe534) or pyrimidines (not shown, clash between extra nitrogen and carbonyl backbones of Phe534 and Asp395) and pyrazines (not shown, same clash as for pyrimidines). A likely explanation would be that even though all were predicted to maintain the pi−stacking interaction with Tyr406, this would be offset by the predicted loss of the cation−pi interaction with Arg536 (Figures 2 and 4).

Five-membered aromatics were also made as a counter-verification of our starting hypothesis, and this class of compounds presented lower potencies since the spacer region was now too short, as predicted from our binding model. Unsurprisingly, the phenyl core **21** was characterized by a poorer ADME profile, whereas 3-pyridine **23** and pyridone **24** were the most interesting cores (most potent cores in ATPlite on the Kasumi-1 cell line, and best LLEs in this series, with Cl_u ∼ 900 mL/min/kg (*iv* PK at 1 mg/kg, Table 4)).

We completed our SAR exploration of the core region with our three most promising heterocycles (pyridazine **14**, 3-pyridine **23**, and pyridone **24**) by adding substituents at the benzylic position (Table 4). Our modeling indicated a possibility to rigidify our scaffold while improving positioning of the hinge region. α-Methylation led to improved potency, while increasing LLE slightly (**14** versus **26**). Racemic syntheses were performed, followed by chiral HPLC separations in the first instance. Cocrystallization of compounds of interest was used to determine the absolute configuration of chiral centers (e.g., **31**, PDB code: 9G4U).

Only a small improvement in potency was typically observed for the absolute configuration between the two diastereomers, which could be explained by modeling. Both α-Me diastereomers of compound **26** (pyridazine core) had comparable, potent interactions with the protein (**26** versus **14**); however, this modification allowed for a clear improvement in free fraction (rfu). The latter finding further translated into improved *iv* PK profiles, as exemplified by inferior unbound clearance values (Table 4) and superior unbound AUC in rat *iv* PK (**31** versus **24** and **32** versus **23**). Most alternative substitutions on our pyridazine core were deleterious to LLE, with increased LogD but identical to lower *in vitro* and *in cellulo* potencies: gem dimethyl **27**, *c*-propyl **28**, ethyl **29**, and trifluoro-methyl **30** were all inferior to **26** (Table 4). This cumulative improvement in potency and

https://doi.org/10.1021/acs.jmedchem.4c02225
J. Med. Chem. 2025, 68, 2981−3003

Table 4. SAR around the Benzylic Substitution of Preferred Cores

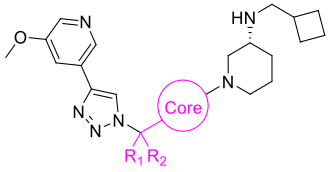

Cpd	Core (hetero)cycle	SPA IC_{50} (nM)	Kasumi-1 IC_{50} (nM)	Log $D_{7.4}$	LLE[a]	rfu	Cl_u[b] (mL/min/kg)	AUC_u[c] (μM.min)
14	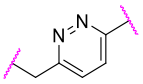	6	1931	1.47	4.24	0.1114	596	5.7
23	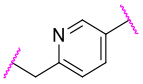	4	894	1.21	4.84	0.0891	934	2.4
24	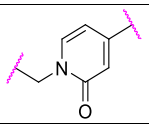	3	1104	1.51	4.45	0.0929	854	2.7
26*	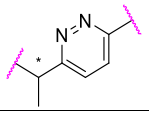	4	904	1.62	4.42	0.1397	423	5.3
27	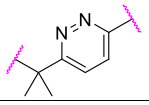	6	2068	1.69	3.99	0.1530	421	4.9
28	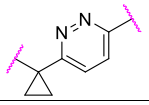	25	9875	1.70	3.31	n.d.	n.d.	n.d.
29*	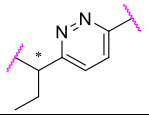	31	6000	1.90	3.35	0.1115	n.d.	n.d.
30*	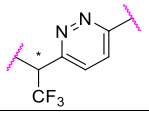	12	12171	2.43	2.48	n.d.	n.d.	n.d.
31	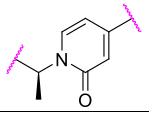	2	489	1.50	4.81	0.1736	645	3.8
32*	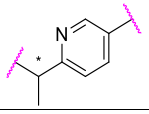	4	2097	1.65	4.03	0.1414	263	10.9

*Most potent diastereomer data provided. [a]LLE = pIC_{50} (Kasumi-1) − LogD. [b]Clu = rat unbound Cl in iv dosing (1 mg/kg/day) = Cl_{total}/rfu. [c]AUCu = rat unbound AUC in iv dosing (1 mg/kg/day) = AUC_{total} × rfu.

unbound PK by α-methylation led to the selection of the pyridone core (**31**) for further optimization (*vide infra*). The clear improvement in potency in **31** was rationalized by solvation of the pyridone core via further stabilization of the carbonyl, through an interaction between the water molecules network and Gln550 (PDB code: 9G4U) and represented an advance in lead optimization relative to the pyridazine core **26**. α-Methylation of **23** afforded a noticeable counter-example with decreased potency (two fold) of most potent diastereomer of **32**, nevertheless still accompanied by strongly improved fraction unbound, as well as *iv* AUC and Cl, which revealed a four fold increased unbound AUC overall versus **23**.

Next, we focused on the five-membered heterocycle of the hinge region (Figure 3). Our hope was to be able to move away from the triazole in anticipation of the feasibility for larger-scale synthesis. Preliminary assessment (DSC and TGA evaluation) of various azide intermediates used to manufacture all core structures of **26**-, **31**-, and **32**-like structures (three pathways investigated for each) showed that those intermediates had potentially hazardous characteristics when heated (significant exothermic transition). We synthesized more than 30 1,2,3-triazole variants overall (with a few different cores), and variations around the preferred core (α-Me-pyridone) of compound **31** are shown in Table 5.

https://doi.org/10.1021/acs.jmedchem.4c02225
J. Med. Chem. 2025, 68, 2981−3003

Table 5. Five-Membered Heterocycle "Hinge" SAR

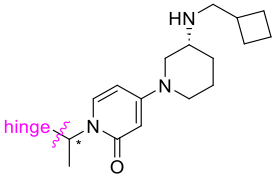

Cpd	Hinge structure	SPA IC_{50} (nM)	Kasumi-1 IC_{50} (nM)	Log $D_{7.4}$	LLE[a]	Cl_u[b] (mL/min/kg)
33*	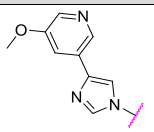	2	453	1.52	4.82	487
34	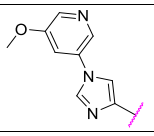	> 30000	> 30000	1.25	< 3.28	n.d.
35*	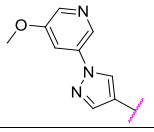	1	306	1.60	4.91	608
36	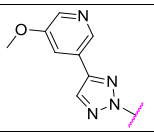	> 30000	> 30000	1.84	< 2.69	n.d.
37*	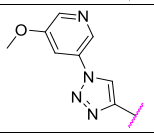	7	1932	1.12	4.59	n.d.
38*	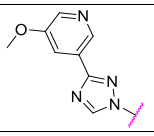	5	1607	1.37	4.42	n.d.
39*	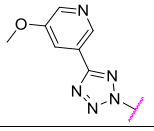	13	5498	1.52	3.74	n.d.
40*	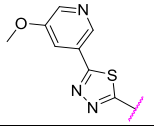	3	506	1.45	4.85	480
41*	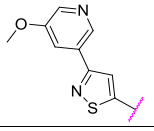	11	1716	2.26	3.51	n.d.
42*	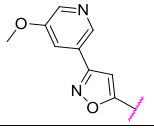	7	1842	1.63	4.10	n.d.

*Most potent diastereomer data provided. [a]LLE = pIC_{50} (Kasumi-1) − LogD. [b]Cl_u = rat unbound Cl in iv dosing (1 mg/kg/day) = Cl_{total}/rfu.

Few of those 1,2,3-triazole replacements showed any advantage with positive exceptions being imidazole **33**, pyrazole **35**, or thiadiazole **40**, even though these compounds were not superior to triazole **31** (same range of potencies in Kasumi-1 ATPlite assay, and of Cl_u). Nonetheless, these exceptions demonstrated that 1,2,3-triazole replacement was feasible. In addition to these five-membered heterocycles described (Table 5), we also synthesized 1,3,4-triazoles, substituted 1,2,3-triazoles, oxadiazoles, 1,2,4-thiadiazoles, various thiazoles and oxazoles, and isomers of imidazoles **33** and of pyrrazoles **35** without success as they were mostly inactive (data not shown). We decided to pursue our optimization with 1,2,3-triazole at this stage of development, as synthetic access was easier, thereby allowing for more rapid SAR exploration.

Lead optimization was completed by evaluation of the pyridine region of our "hinge" moiety, with the aim to identify a more potent inhibitor *in cellulo* as a proof-of-concept compound adequate for *in vivo* studies (see further below). A few representative examples of compounds made around the α-Me-pyridone core of **31** are depicted in Table 6. 6-Methoxyindazole version analogue of compound **31** was made (**43** in Table 6 below) and showed improved inhibition, but with an inferior ADME/PK profile (anticipated from decreased LLE). We quickly focused our efforts on pyridine moieties, as alternative fused bicyclic analogues have not delivered improved potency, while their ADME profile was compromised with lipophilic bis-aryls (**44** as single example shown). Compound **45** confirmed that nitrogen at the 3-position on our pyridine was crucial for activity, as clearly identified in SAM cocrystals (PDB: 5IL1) via strong interaction between SAM purine nitrogen with Ile378 backbone, in addition to pi-stacking with Phe534 and further purine NH_2−Asp377 interaction (Figure 4). These three main interactions were all reproduced by the indazole moiety in compound **1** (as well as with the UZH1a compound).

Electron-donating groups in the meta-position were indispensable to reinforce electron density at the nitrogen atom in the pyridine and to allow for efficient binding (**31** > **46** > **47**). Methoxy **31** and the ethoxy analogue **49** were the most potent examples of this series. Analogue **49** has increased LogD versus **31**, which translates into a two fold decrease in rfu, affording an approximate two fold increase in the rate of unbound clearance and, consequently, about half the exposure (unbound AUC). 6-Methoxypyridin-3-yl in **48** (methoxy group in the α position to the nitrogen of the pyridine) confirmed the electronic trend above and most likely resulted in an additional steric clash with the METTL3 loop in close proximity. Pyridazine **50** was less tolerated as well (lone pair repulsion), while pyrazine **51** was equipotent as one would expect but with a deteriorated CYP profile (predominantly 2D6 inhibition). This electronic trend was confirmed by the 3-amino-pyridine variants proving to be the most potent and interesting compounds (**52** and **53** as representatives, Table 6). Pyrrolidine **53** demonstrated a good fit for the lipophilic pocket of METTL3 and also had improved permeability (one of our best IC_{50} *in cellulo* on the Kasumi-1 cell line). The *N,N*-dimethyl variant of pyrazine **51**, analogue **54,** proved to have ameliorated Cl_u and AUC_u. Additional amino-based cycloalkyls (not shown) and heteroaryls (such as **55**) were made and showed decreased potency. Finally, disubstituted pyridin-3-yl analogs were as synthesized but did not yield compounds with improved profiles (not shown). Both dimethylamine-pyridine **52** and the pyrazine **54** showed improved inhibition of Kasumi-1 (>10-fold) *in cellulo* against methoxy variant **31**, with improved LLE by at least 0.8 log unit, and unbound AUC in rat *iv* PK in the same range. Compound **53**, bearing a pyrrolidine, was the most potent with a 30−72-fold improve-

https://doi.org/10.1021/acs.jmedchem.4c02225
J. Med. Chem. 2025, 68, 2981−3003

Table 6. Pyridine "Hinge" SAR

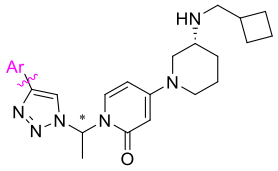

Cpd	Ar	SPA IC_{50} (nM)	Kasumi-1 IC_{50} (nM)	Log $D_{7.4}$	LLE[a]	Cl_u[b] (mL/min/kg)	AUCu[c] (μM.min)
43*	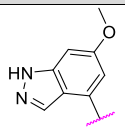	2	437	2.13	4.23	2269	0.9
44*	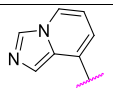	8	5401	1.53	3.74	n.d.	n.d.
45	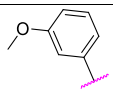	198	> 30000	2.22	< 2.31	n.d.	n.d.
46		39	8121	0.87	4.22	n.d.	n.d.
47	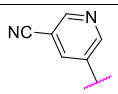	110	> 30000	0.97	< 3.56	n.d.	n.d.
48	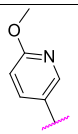	> 30000	> 30000	1.69	< 2.84	n.d.	n.d.
49*	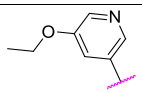	2	302	2.07	4.45	1112	2.1
50*	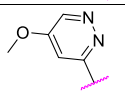	5	5415	0.62	4.65	n.d.	n.d.
51*	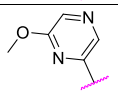	3	656	1.65	4.53	413	6.1
52*	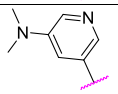	2	44	1.79	5.57	803	2.2
53*	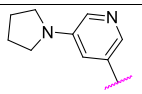	2	7	2.49	5.67	1913	1.0
54*	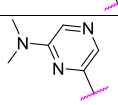	1	35	1.69	5.78	449	4.7
55*	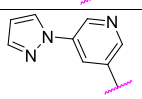	2	301	1.80	4.72	529	3.3

*Most potent diastereomer data provided. [a]LLE = pIC_{50} (Kasumi-1) − LogD. [b]Cl_u = rat unbound Cl in iv dosing (1 mg/kg/day) = Cl_{total}/rfu. [c]AUCu = rat unbound AUC in iv dosing (1 mg/kg/day) = AUC_{total} × rfu.

ment in potency for inhibition in ATPlite assays but compromised by a decreased unbound AUC by nearly four fold, thereby limiting its pharmacokinetic suitability. Overall, we selected **52**, **53**, and **54** as our best compounds in this series and best templates before the last round of optimization.

To further improve the PK profile of our compounds **52** to **54**, we used the SAR knowledge we had generated based on the cycloalkylamine moiety. The most interesting result was the size reduction from *c*Bu of **1** to the *c*Pr **11** analogue. This small apparent change had a minimal effect on potency as measured by SPA and ATPlite, while improving the ADME

https://doi.org/10.1021/acs.jmedchem.4c02225
J. Med. Chem. 2025, 68, 2981−3003

Table 7. Fine Tuning around Compound 52

Cpd	Structure	SPA IC_{50} (nM)	Kasumi-1 IC_{50} (nM)	Log $D_{7.4}$	LLE[a]	Cl_u[b] (mL/min/kg)	AUCu[c] (μM.min)
56	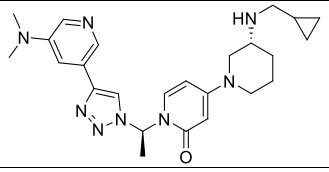	2	37	1.16	6.28	358	5.1
57*	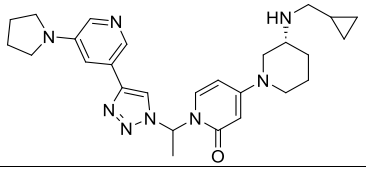	3	11	1.93	6.04	1487	1.3
58*	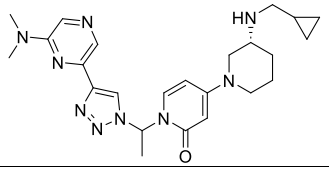	1	96	1.17	5.87	369	5.2
59	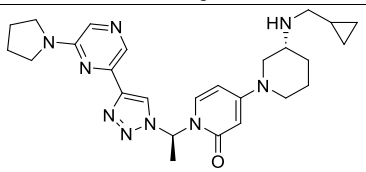	1	13	1.60	6.29	443	4.7

*Most potent stereoisomer data provided. [a]LLE = pIC_{50} (Kasumi-1) − LogD. [b]Cl_u = rat unbound Cl in iv dosing (1 mg/kg/day) = Cl_{total}/rfu. [c]AUCu = rat unbound AUC in iv dosing (1 mg/kg/day) = AUC_{total} × rfu.

profile (PPB and CYPs) and unbound PK parameters (better LLE as well). Application of this modification to our best template compounds provided **56** to **59** that offered the best overall profiles in this series (Table 7). Absolute configurations of **56** and **59** were confirmed by cocrystallization with truncated METTL3/14 protein (PDB codes: 9G4S and 9G4W). We selected compound **56** as our proof-of-concept compound for *in vivo* experiments (*vide infra*) since *in cellulo* inhibition was improved together with better, overall global lipophilicity (ΔLLE > 0.7), PPB, and ultimately an improvement in unbound PK parameters by nearly three fold (Cl_u and AUC_u; see Table 7).

Crystallographic Observations. As cited above, some of the most promising analogues (e.g., **31**, **56**, and **59**) had binding hypotheses confirmed by X-ray crystallography, and surprisingly, new loop configurations were observed with cyclopropyl-substituted amines (Figure 5A). In contrast, cyclobutyl analogues adhere to the existing patterns observed for other literature example chemotypes (Figure 5B shows the new loop positioning of our cocrystallized structure of **56** (pink), versus cocrystals published with STM2457 (green), and UZH2 (blue)). On closer inspection of the crystallographic results, it is apparent that engagement with Trp431 (Figure 5A), which is a key component of SAR around the Storm Therapeutics and Caflisch chemotype SAR, is consistent with a shift in this proximal loop. The cyclopropyl analogues, however, are small enough to accommodate an alternative loop configuration while making similar interactions with Trp431, but via a geometrically more compact loop configuration (Figure 5A, magenta residue). The overall trajectory of this highly flexible loop and its pendent residues is impacted significantly by this small change. An equivalent interaction was highlighted with His512 (magenta residue in Figure 5A) pointing to the ligand (interaction with core aromatic) when *c*Pr was in place, instead of Arg536 interacting with core aromatic in all other published structures (yellow residue in Figure 5A), pushing away His512. We hypothesized that the presence of *c*Pr stabilizes this loop and allows equivalent interaction with the pyridone core.

Biological Evaluation of EP652. Extensive profiling was carried out on the preferred compound **56** (also known as **EP652**) in consideration of its suitability for advancement into *in vivo* studies. The **EP652** ADME profile is summarized in Table 8 and shows a suitable profile for use as an *in vivo* proof-of-concept compound: high unbound fractions in both rat and mouse plasma as well as promising metabolic stability as measured in rat and human liver microsomes and hepatocytes. hERG binding of **EP652** was also evaluated, and no inhibition was measured up to 30 μM. The pharmacological and pharmacokinetic profile of **EP652** is presented in Table 9 in comparison with **STC-15** (Figure 1), as the latter compound is reported to have efficacy in mouse cancer models. **EP652** demonstrated consistent efficacy *in cellulo* across various cell lines (typically >30-fold more potent in Kasumi-1 and MV-4−11 (AML cell lines), Caov-3 and SK-OV-3 (ovarian cancer cell lines), Calu-6 and A549 (lung cancer cell lines), and FaDu (Head and neck cancer cell line)) in cell viability experiments as well as in a spheroid model of 3D cell proliferation (NCI-H1650, lung cancer cell line). The antiproliferative effects of **EP652** correlated with its concentration-dependent reduction of intracellular m^6A as an epigenetic marker on mRNA as measured in cell-based assays on various AML and solid tumor cell lines (Calu-6 presented as an example, Figure 6). **EP652** further demonstrated superior induction of apoptosis in

https://doi.org/10.1021/acs.jmedchem.4c02225
J. Med. Chem. 2025, 68, 2981−3003

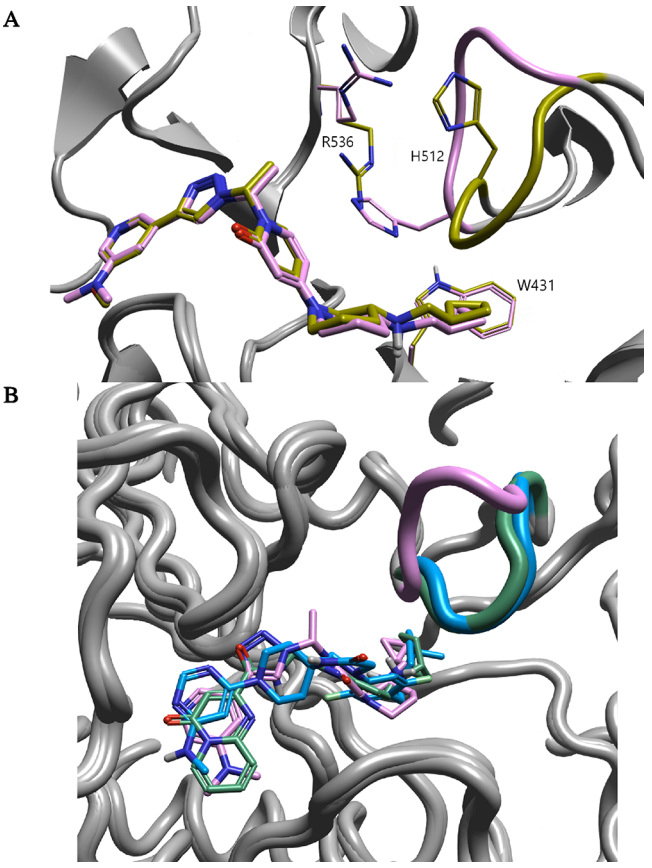

Figure 5. (A) Loop positioning with *c*Bu subseries in yellow (**31** shown) *versus* *c*Pr subseries in pink (**56** shown). (B) Comparison of loop positioning between Storm reference compound STM2457 (green), UZH2 (blue), and our compound **56** (pink).

Table 8. EP652 ADME Profile

ADME profiling assay	EP652
rfu	0.23
mfu	0.20
RLM $T_{1/2}$	91.3 min
HLM $T_{1/2}$	140.7 min
rat hepato stability	>240 min
human hepato stability	>240 min
CYP inhibition (IC_{50}, μM): 1A2/2C19/2C9/2D6/3A4	>100/> 100/> 100/> 100/0.9
HepG2 viability at 50 μM	90.3%
hERG binding IC_{50}	>30 μM

Table 9. Comparison of Compound 56 (EP652) and STC-15

	EP652	STC-15
SPA IC_{50} (nM)	2	4
Cell viability (APTlite, IC_{50} (nM), 72 h):		
Kasumi-1	37	1156
MV-4-11	234	7633
Caov-3	20	563
Calu-6	18	1145
A549	169	>5000
FaDu	50	2214
SK-OV-3	11	371
Spheroid model (NCI-H1650) IC_{50} (nM):	99	2061
Log $D_{7.4}$	1.16	1.90
LLE[a]	6.28	4.05
intracellular m^6A IC_{50} (nM):		
Kasumi-1	5	138
MV-4-11	5	182
Calu-6	9	169
A549	7	264
FaDu	6	331
SK-OV-3	3	134
iv rat (1 mg/kg) AUCu[b] (μM·min)	5.1	4.6
ip mouse (30 mg/kg) AUCu[b] (μM·min)	175.8	298.1

[a]LLE = pIC_{50} (Kasumi-1) − LogD. [b]AUCu = unbound AUC = AUC_{total} × r/mfu.

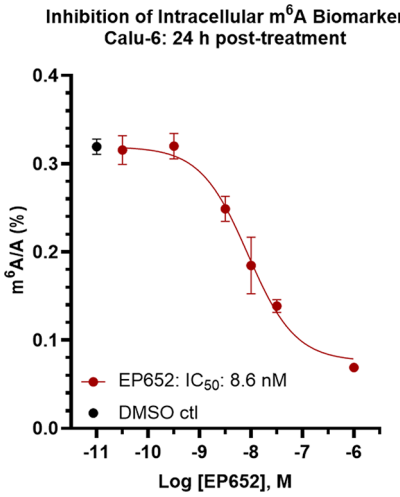

Figure 6. m^6A inhibition of **EP652** in mRNA from Calu-6 after 24 h treatment.

Kasumi-1 and MV-4−11 cell lines (see the Supporting Information). Pharmacokinetic profiling indicated that the unbound free fraction of **EP652** is sufficient to anticipate METTL3 target coverage (based on *in cellulo* potencies) at relevant dose ranges to be used in mouse cancer models. Overall, the comparative profiling of **EP652** versus **STC-15** together with the pharmacokinetic exposure of **EP652** justified its advancement into *in vivo* cancer models.

In addition, we demonstrated the METTL3/14 selectivity of **EP652** inhibition (at 10 μM) against a panel of 40 methyltransferases (Figure 7, and complete details in the Supporting Information) and FTO (main m^6A demethylase). Also, **EP652** was evaluated in a standard safety screen panel (44 targets, including GPCRs, ion channels, and kinases), which further demonstrated METTL3 target selectivity with no significant off-target affinity nor inhibition at 10 μM concentration (>500-fold selective relative to enzymatic inhibition of METTL3/14 (IC_{50} < 2 nM (SPA), see the Supporting Information).

Before moving to *in vivo* efficacy tumor models, we assessed *in vivo* target engagement with **EP652** following intraperitoneal administration of **EP652** to rats and subsequent collection of buffy coat for isolation and quantification of cellular m^6A levels relative to both vehicle-treated and reference (**STC-15**)-treated controls (Figure 8). Clinical compound **STC-15** clearly showed a dose-dependent decrease of the m^6A cellular level in PBMC (up to 61%) from 3 to 30 mg/kg, while our proof-of-concept compound **EP652** demonstrated maximum m^6A reduction (~75%) at as low as 0.3 mg/kg. Historical data accrued at EPICS from numerous concentration−response

https://doi.org/10.1021/acs.jmedchem.4c02225
J. Med. Chem. 2025, 68, 2981−3003

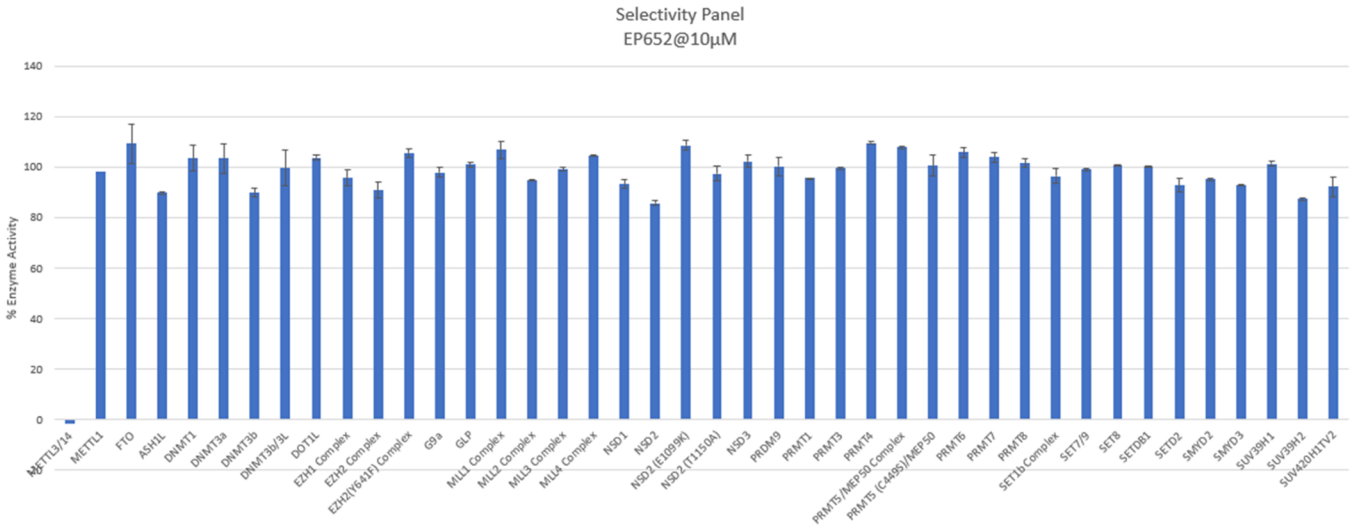

Figure 7. EP652 inhibition of methyltransferases at 10 μM (duplicates) and FTO demethylase.

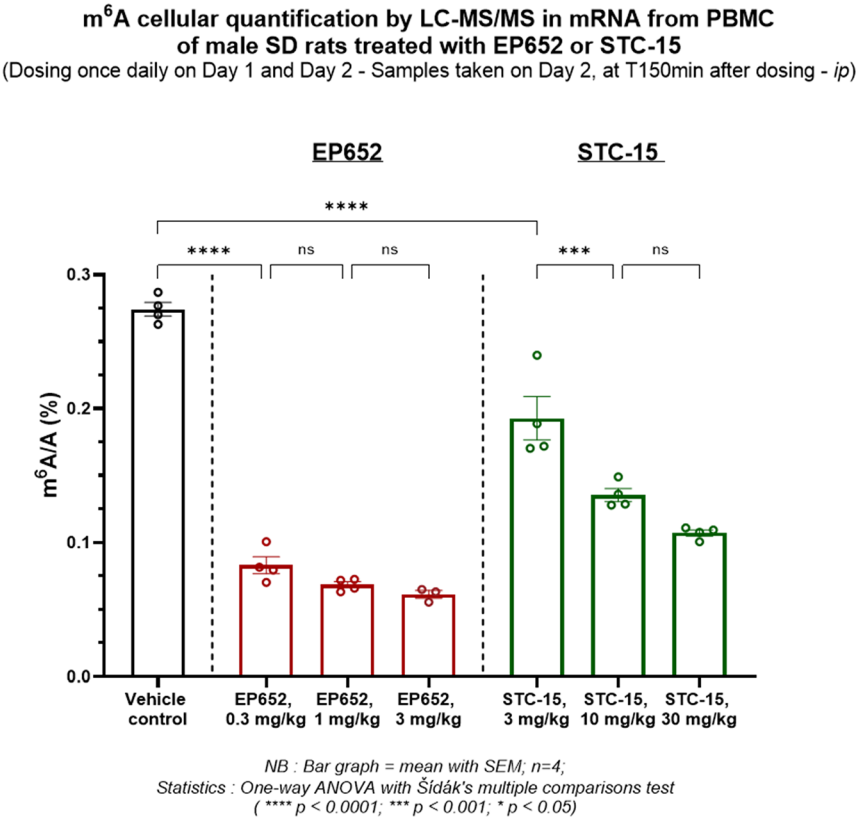

Figure 8. m^{6}A cellular quantification in mRNA from PBMC after treatment with **EP652** or **STC-15**.

experiments (conducted with different METTL3 inhibitors, both *in vitro* and *in vivo*) consistently indicates that the maximal, achievable reduction of m^{6}A/A is typically in the range of ∼80%, which is corroborated by findings in the literature following CRISPR/Cas9-knockdown of METTL3.[31] **EP652** treatment elicited this maximal level of reduction of m^{6}A/A over the concentration range tested and demonstrated superior potency to **STC-15** in this assay. In total, these *in vitro*, pharmacokinetic, and *in vivo* target engagement data demonstrate the suitability of **EP652** as a candidate for testing in *in vivo* cancer models.

EP652 was tested *in vivo* in an orthotopic, patient-derived xenograft model of AML (LEXFAM 4128, intratibial implantation, female NSG mice). **EP652** was dosed at 30 mg/kg, *ip*, QD for 91 days and was shown to significantly prolong survival ($p < 0.01$, relative to vehicle control) up to study conclusion (by protocol) on day 112 (Figure 9).

These initial results were confirmed in another disseminated xenograft model of AML using an established systemic MV-4-11 model (MV-4-11-Luc-mCh-Puro CDX model). Female NSG mice were subjected to intravenous implantation of 2 × 10^6 cells (AML), and **EP652** treatment (30 mg/kg, *ip*, QD for 31 days) was initiated 5 days post-implant versus vehicle-

https://doi.org/10.1021/acs.jmedchem.4c02225
J. Med. Chem. 2025, 68, 2981−3003

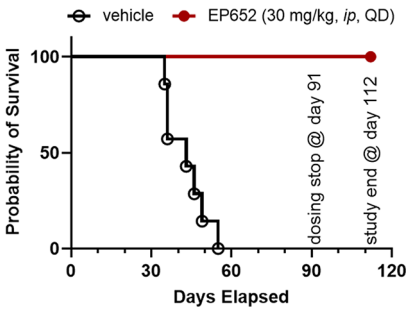

Figure 9. EP652 efficacy in the LEXFAM 4128 mouse model (N = 6−7 mice/group).

treated control. The main study arms were subjected to imaging (bioluminescence imaging (BLI)) once weekly up to day 40 (Figure 10A). **EP652** effectively inhibited cancer progression as measured by in-life imaging. Satellite groups of mice (N = 5/group) were terminated on day 28 of this study for tissue collection, and analysis of by flow cytometry indicated selective decreases of hCD45$^+$ (human, cancer cells) in bone marrow, blood, and spleen, corroborating the imaging results that **EP652** treatment effectively arrested cancer progression (Figure 10B). An additional experiment was run in the same model where **EP652** was tested at 10 and 30 mg/kg *ip*, QD, and BLI was reported on day 19 indicative of a dose-dependent response (Figure 10C).

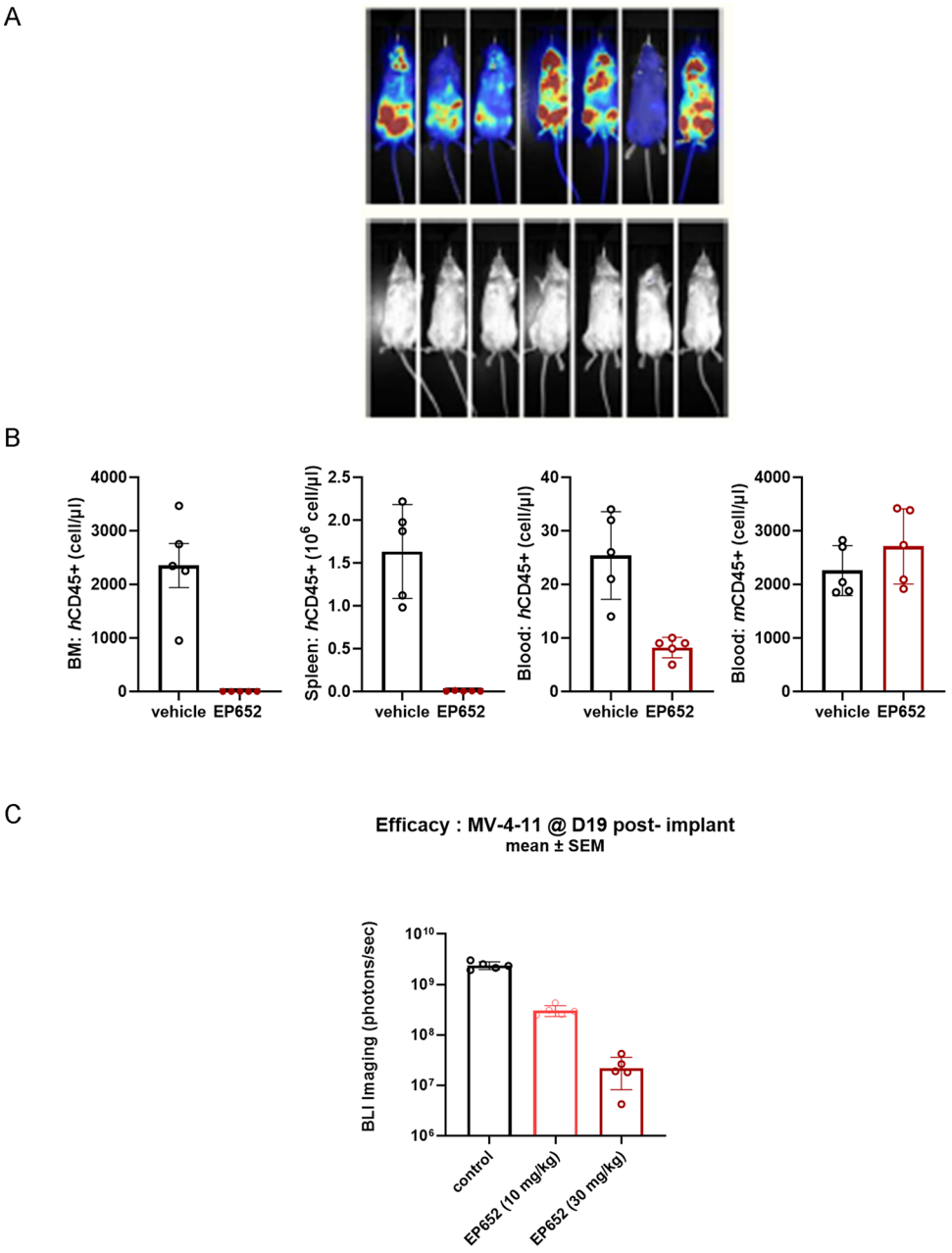

Figure 10. (A) Bioluminescence imaging (day 40, post-implant) of AML cells, vehicle (upper) versus **EP652** treated (30 mg/kg, *ip*, QD, lower). (B) Flow cytometry shows that **EP652** treatment selectively decreases hCD45$^+$ cells on bone marrow, spleen, and blood (p < 0.05). (C) Bioluminescence imaging (day 20, post-implant) with **EP652** at 10 and 30 mg/kg *ip*, QD, shows a dose-dependent response.

https://doi.org/10.1021/acs.jmedchem.4c02225
J. Med. Chem. 2025, 68, 2981−3003

The efficacy of **EP652** was further examined in solid tumor models. In addition to AML cell lines above (Table 8), the antiproliferative effects of **EP652** were measured in cell viability assays following a 72 h treatment of A549[32] (NSCLC, IC_{50}: 169 nM), SK-OV-3[33] (ovarian, IC_{50}: 11 nM), and FaDu[34] (hypopharyngeal squamous cell carcinoma, IC_{50}: 50 nM) cells. Complementary data in all three cell lines demonstrate a clear concentration−response for a target engagement biomarker (m^6A inhibition, Table 9). In addition, biomarkers of METTL3 inhibitor compound activity were evaluated on samples collected from treated cells and showed that downstream effects on biomarkers correlated with METTL3 inhibitor compound activity (Figure 11) as **EP652** induced changes in the biomarkers of oncogenic drivers. Bcl-2, a well-known oncogenic driver, and Bax, a pro-apoptotic driver, were respectively downregulated and upregulated upon treatment with **EP652** (tested at the IC_{50} concentration determined in corresponding viability assay for each cell line, Table 8).

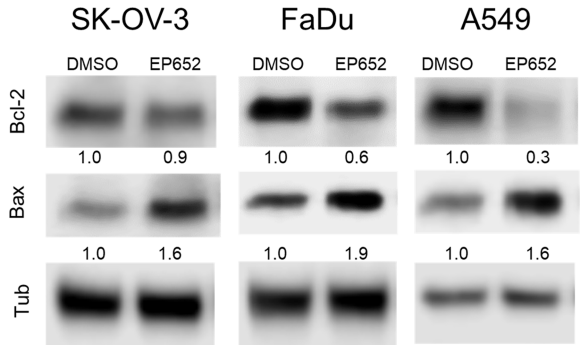

Figure 11. Biomarkers effect after 72 h of treatment with **EP652** on various solid tumor cell lines.

EP652 (30 mg/kg, *ip*, QD) was then tested *in vivo* in mouse models using FaDu (subcutaneous implant) in addition to A549 and SK-OV-3 (both orthotopic implants), and **EP652** treatment significantly prolonged survival in all three disease models, consistent with efficacy on tumor growth inhibition as measured by imaging or direct measurement of tumor volume in the case of subcutaneous implant (FaDu). Survival curves in the FaDu and NSCLC models (A549) are presented in the supplemental data. In the ovarian cancer model (SK-OV-3, orthotopic implant), bioluminescence measurements (Figure 12A) clearly showed tumor growth inhibition over the course of treatment with **EP652** (30 mg/kg, *ip*, QD) with imaging presented (Figure 12B) for day 52 (the latest time point with a full complement of surviving mice in the vehicle group). Inhibition of tumor growth corresponded to an improved survival in response to treatment with **EP652** (Figure 12C). Effects on body weight gain were minimal in response to **EP652** drug treatment, and furthermore, there were no observations of macroscopic adverse events over the treatment period.

In summary, chimerization and scaffold hopping from early published structures delivered a starting point for lead optimization (**compound 1**) culminating in the novel METTL3 inhibitor, **EP652**, via a structure-based and LBDD approach. This compound exhibited a favorable profile to potently inhibit METTL3 and correspondingly inhibit cancer cell proliferation across a broad range of *in cellulo* models, encompassing both solid tumors and hematological cancers. Efficacy in *in vitro* models translated to *in vivo* efficacy on

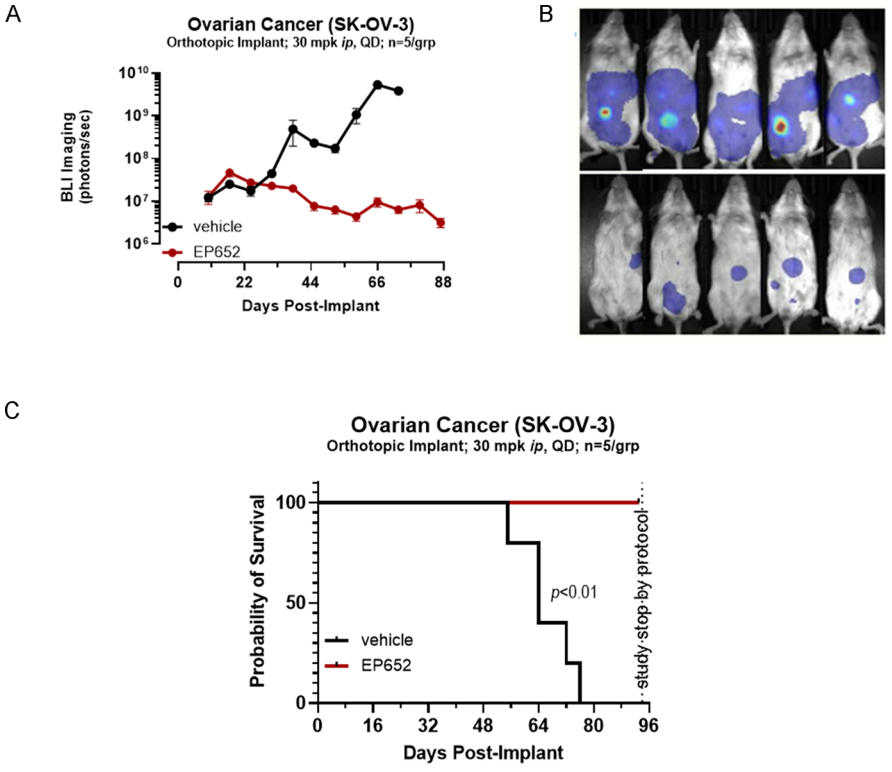

Figure 12. (A) Bioluminescence time course during treatment with **EP652** in the SK-OV-3 model. (B) Imaging (day 52 after the orthotopic implant) of SK-OV-3 cells: vehicle (upper) versus **EP652** (lower, 30 mg/kg, *ip*, QD). (C) Survival curves upon **EP652** treatment.

https://doi.org/10.1021/acs.jmedchem.4c02225
J. Med. Chem. 2025, 68, 2981−3003

Scheme 1. Synthetic Access to Most of Compounds in Tables 1 and 2

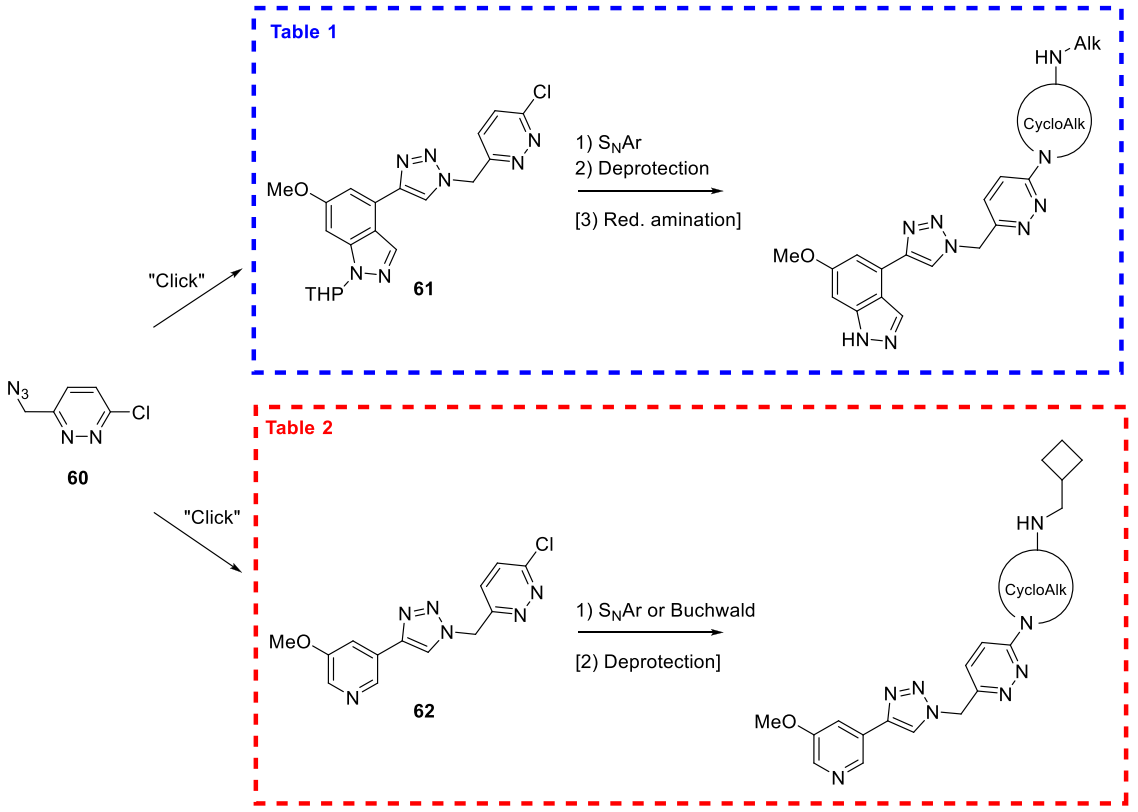

Scheme 2. Synthetic Access to Core Variations in Table 3

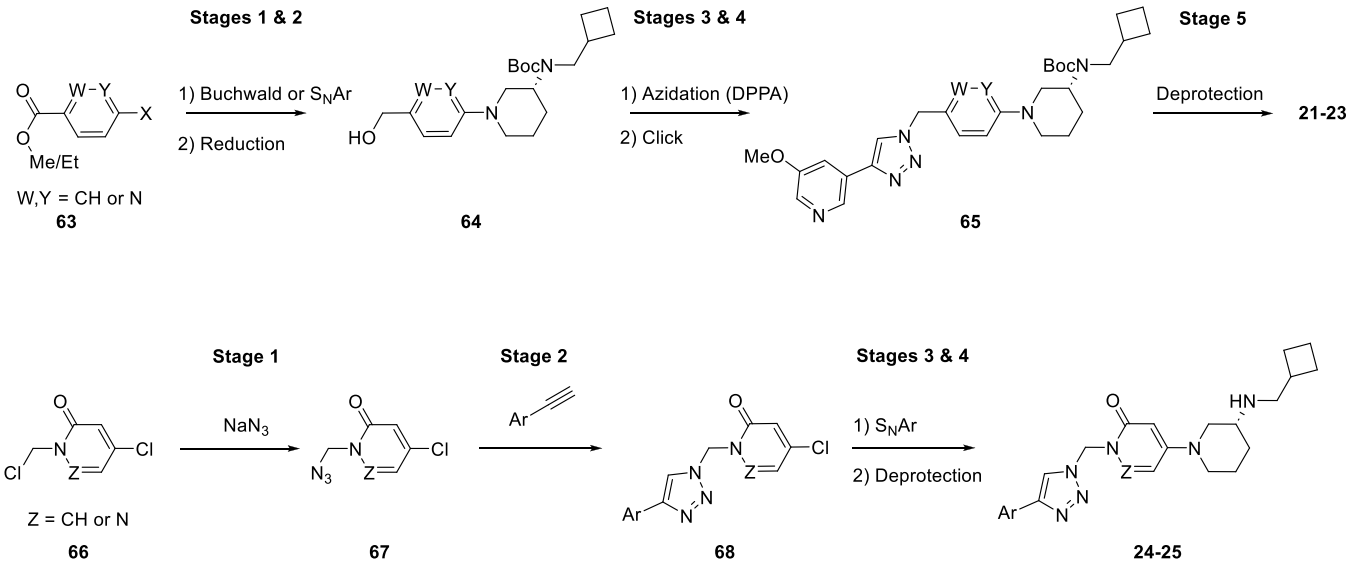

tumor growth inhibition in both CDX and PDX models of AML, as well as in various solid tumor models, whereupon the results in SK-OV-3 (ovarian cancer) are highlighted in this report. These data provide further evidence that pharmacological inhibition of METTL3 is a viable approach for the treatment of cancer.

Chemistry. The development of **EP652** stems from the identification of two main pathways during the retrosynthetic analysis of our hit **1**: namely, permitting the introduction of the hinge first by click chemistry and then introduction of the piperidine moiety by aromatic nucleophilic substitution (S_NAr), or the inversion of these two main steps by introducing first the piperidine to complete the target by building the triazole. The first approach (Scheme 1) was mainly used as the chiral piperidine building block was our more valuable and limiting reagent in these medicinal chemistry syntheses. We started from the easily accessible 3-(azidomethyl)-6-chloropyridazine **60** to access most of the compounds from Tables 1 and 2 (full details in the Supporting Information). Click chemistry allowed quick access to chloropyridazines **61** and **62**, and aminocycloalkyls were then introduced either by aromatic nucleophilic substitution

https://doi.org/10.1021/acs.jmedchem.4c02225
J. Med. Chem. 2025, 68, 2981−3003

Scheme 3. Access to α-Substituted Pyridazines and 3-Pyridine

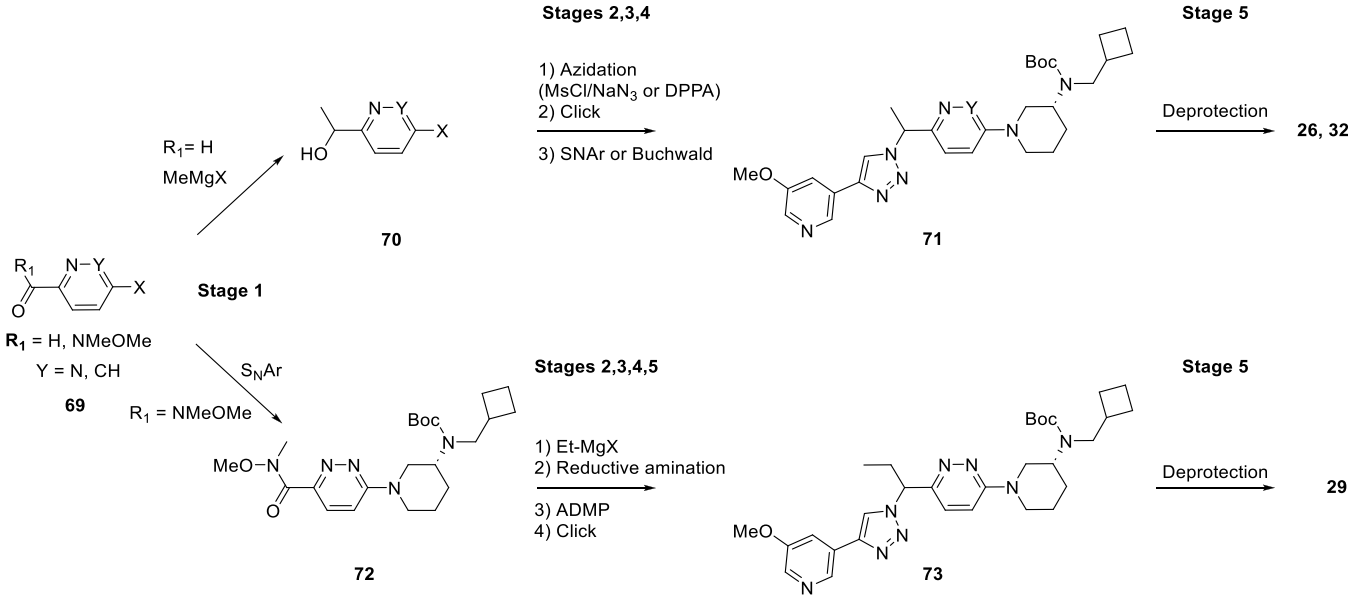

or C−N Pd-catalyzed crosscoupling ("Buchwald" reaction). Finally, simple Boc deprotection, when needed, completed the syntheses. Additionally, reductive amination could be used as the last step to quickly derivatize this aminoalkyl moiety (Table 1).

Compounds **1** and **2** were made using S_NAr from **61** and the corresponding chiral *tert*-butyl (cyclobutylmethyl)(piperidin-3-yl)carbamate, while compound **4** was obtained by alkylation of **1**. Compounds **3** and **6**−**9** were accessed by either acylation (for **3**), or reductive amination on compound **5**, where the latter product was simply obtained from nonalkylated *tert*-butyl (*R*)-piperidin-3-ylcarbamate S_NAr, followed by Boc-deprotection in acidic conditions. For **10** and **11**, corresponding alkyl groups were introduced on the chiral piperidine building block first before S_NAr, and the resulting intermediates were Boc deprotected to deliver our targets. Syntheses of compounds **12** and **13** were performed analogously by exchanging the piperidine building block by corresponding *tert*-butyl (cyclobutylmethyl)(pyrrolidin-3-yl)carbamate (**12**), or *N*-(cyclobutylmethyl)piperidin-4-amine (**13**).

Compound **14** was the only compound in Table 2 obtained using the "inverted" pathway eluded above: a phthalimide analogue to **60** was used to introduce first the piperidine moiety through S_NAr, and then protected amine was transformed into azide, followed by click reaction and final Boc deprotection. Other close analogues from Table 2 were synthesized using the same approach as for Table 1 compounds (Scheme 1, bottom part). Intermediate **62** was easily obtained and carried on using S_NAr to access Boc-protected intermediates, followed by deprotection to reach **15**−**17** (full details in the Supporting Information). Homologated piperidine building block *tert*-butyl (*S*)-(piperidin-3-ylmethyl)-λ2-azanecarboxylate provided an intermediate toward compound **20** after Boc deprotection and reductive amination. Cyclohexyl variant **18** was obtained by the same final sequence as **20**, after Suzuki coupling with the corresponding Boc-amino-cyclohexene pinacol boronic ester. Finally, piperidone **19** was easily obtained through Buchwald coupling from the piperidone building block variant and still Boc deprotection.

Core variations in Table 3 were accessed by the opposite approach (Scheme 2) for phenyl **21** and pyridines **22** and **23**. The piperidine moiety was introduced first by either Buchwald coupling or S_NAr (for 2-pyridyl **22**) on difunctionalized aromatics **63**. Following ester reduction, intermediate alcohols **64** were transformed into azide using DPPA and click reaction was performed to afford intermediates **65**. Final Boc deprotection provided **21**−**23**. For pyridone **24** and pyridazinone **25**, triazole formation was carried on at first stages, followed by S_NAr and deprotection as depicted in Scheme 2.

The alkylated analogues in pseudobenzylic position depicted in Table 4 were obtained by conventional methods (Scheme 3). In the case of α-methylated targets **26** and **32**, methyl was introduced on aldehyde-halogeno-pyridine or pyridazine **69**. The corresponding alcohols **70** were activated and azide was added, followed by click reaction and then S_NAr or Buchwald reaction. As described above, Boc deprotection of **71** completed the syntheses of **26** and **32**. The mixture of diastereomers obtained were separated using preparative chiral HPLC. α-Ethyl was introduced on Weinreb amide **72** after S_NAr had been conducted. The corresponding ketone was transformed into azide in a two-step sequence of reductive amination, followed by azide formation using ADMP.[35] Click reaction delivered intermediate **73**, which was deprotected to afford **29**, which was ready for chiral preparative HPLC separation.

Dimethylated compound **27** was obtained through use of Ellman sulfinamide onto the methyl ketone. Further addition of MeMgBr and deprotection provided the corresponding amine. Synthesis was completed as described above for **29** (see the Supporting Information for full details). Last, for CF_3 analogue **30**, introduction onto aldehyde **69** was performed using a Ruppert−Prakash reagent. Corresponding pyridazine-alcohol was reacted with piperidine building block first and then OH-activation, azide addition, and click reaction delivered **30** as a mixture of two diastereomers after Boc deprotection. As above, the latter were separated by chiral preparative HPLC. α-Methyl pyridone **31** was made like **24** in Scheme 2, simply by using 1-chloroethyl chloroformate to

https://doi.org/10.1021/acs.jmedchem.4c02225
J. Med. Chem. 2025, 68, 2981−3003

Scheme 4. General Scheme toward α-Methyl Pyridone Targets

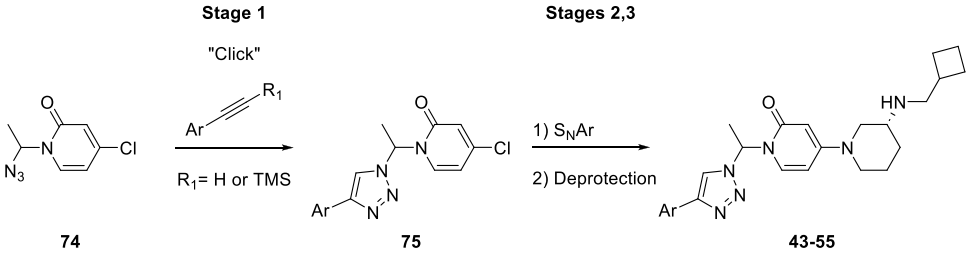

introduce α-methyl onto 4-chloropyridone. Then, the sequence was identical to provide **31** as a mixture of diastereomers, ready for chiral preparative HPLC separation. The absolute configuration was assessed by cocrystallization with truncated METTL3/14 protein complex (PDB code: 9G4U).

Compounds depicted in Table 5 were all quite challenging to make for various reasons (stability, solubility of intermediates, regioisomerism, etc.). All these syntheses were tailor-made and often not efficient. They are described in detail in the Supporting Information.

As explained above, our focus was then on the α-methyl pyridone core. All compounds made and illustrated in Table 6 were synthesized based on compound **24** synthesis (Scheme 2), after introduction of the methyl as explained for **31** above (general pathway in Scheme 4).

Protected alkynes were typically made easily via the Sonogashira coupling reaction. Then, racemic intermediate **74** was reacted either in typical catalytic click chemistry reaction using CuI and deprotected alkyne (R_1 = H) or using stoichiometric CuF_2 with TMS-protected alkynes via *in situ* deprotection. The latter method had the advantage of avoiding handling volatile or unstable alkynes but used stoichiometric copper reagent. Following S_NAr and deprotection were easily achieved as explained above from intermediates **75** to deliver **43**−**48**, **50**−**52**, and **54**,**55**. Compounds **49** and **53** were obtained through S_NAr reaction from the 3-fluoro-pyridine analogue with NaOEt or pyrrolidine, respectively, before Boc deprotection. The most potent diastereomeric mixtures were separated by chiral preparative HPLC.

Finally, "fine-tuned" compounds in Table 7 were obtained by the same pathway, exemplified below by the small scale-up medicinal chemistry synthesis of our proof-of-concept compound **56**/**EP652** (Scheme 5). The latter was efficient at each step but final chiral separation and allowed us to deliver a nearly 7 g batch.

CONCLUSIONS

We describe the discovery by chimerization and scaffold hopping of our initial hit **1**, culminating in the selection of compound **56** (**EP652**) for *in vivo* studies based on its favorable profile after extensive structure-based design approaches and multiparameter optimization. This compound shows high selectivity against 40 methyltransferases and an adequate safety margin in a broad safety screening panel of various target classes as well as no inhibition of hERG. **EP652** was successfully scaled up to multigram-scale synthesis thanks to an efficient medicinal chemistry pathway. The results presented herein confirmed that the pharmacological inhibition of METTL3 could be a viable strategy for the treatment of AML. The proof-of-concept compound **EP652** has been shown to be effective in mouse CDX and PDX models of AML by prolonging survival and inhibiting cancer progression. Furthermore, **EP652** is also effective in attaining tumor growth inhibition against select types of solid tumors, whereupon we highlight the results obtained in the SK-OV-3 model. The efficacy of **EP652** as a single agent on tumor growth inhibition and survival advances the validation of METTL3 as a cancer target and provides additional evidence of the applicability of mRNA epigenetic mechanisms to the treatment of AML and solid tumors. Although **EP652** is an advanced compound to explore METTL3 pharmacology *in vivo*, it is best suited to peripheral dosing routes. Continued optimization of this lead series is focused on the delivery of superior, orally available compounds, and such results will be reported in due course.[36]

EXPERIMENTAL SECTION

General Information. All reactions were performed under an argon atmosphere at RT using anhydrous grade solvents, except as otherwise noted. All reagents were used as supplied by the vendor, except as noted. Analytical thin-layer chromatography (TLC) was performed on a Merck silica gel 60 (230−400 mesh). NMR spectra were recorded on a Bruker ARX spectrometer (300 MHz) at RT. Coupling constants (J) are expressed in hertz (Hz). Chemical shifts (δ) are expressed in parts per million relative to the residual solvent as an internal reference. Peak multiplicities are expressed as follows: singlet (s), doublet (d), triplet (t), quartet (q), pentaplet (p), hexuplet (h), heptuplet (hept), multiplet (m), and broad singlet (bs). HPLC purity analysis was carried out using one of the following methods. Method A: LC/multiwavelength detector coupled to single quadrupole mass spectrometry detector (LC/UV/MS); column: SunFire C18 3.5 μm 3.0 × 50 mm; mobile phase A: 0.1% TFA in water (v/v); mobile phase B: 0.1% TFA in CH_3CN (v/v); gradient begins at 5% B, hold 0.2 min at 5% B, increasing to 95% B over 6.0 min, hold at 95% B until 7.75 min; flow rate: 1.0 mL/min. Method B: LC/multiwavelength detector coupled to single quadrupole mass spectrometry detector (LC/UV/MS); column: SunFire C18 3.5 μm 3.0 × 50 mm; mobile phase A: 0.1% TFA in water (v/v); mobile phase B: 0.1% TFA in CH_3CN (v/v); gradient begins at 5% B, hold 0.2 min at 5% B, increasing to 95% B over 1.8 min, hold at 95% B until 3.75 min; flow rate: 1.0 mL/min. All final compounds are ≥95% pure by HPLC analysis or ^{1}H NMR when HPLC was not appropriate. PerkinElmer ChemDraw Professional software (version 22) was used for naming the compounds described below.

*N,N-Dimethyl-5-((trimethylsilyl)ethynyl)pyridin-3-amine (**78**).* To a mixture of **76** (10.60 g, 52.72 mmol), copper(I) iodide (0.34 g, 1.75 mmol), and ethynyltrimethylsilane **77** (9.25 mL, 63.43 mmol) in anhydrous THF (105 mL) was added triethylamine (106 mL, 756.71 mmol). The mixture was degassed by argon bubbling for 5 min. Bis(triphenylphosphine)palladium(II) chloride (1.13 g, 1.57 mmol) and triphenylphosphine (1.26 g, 4.80 mmol) were added, and the reaction mixture was heated to 65 °C for 16 h. The solution was then cooled to RT, filtered on a Celite pad. Solid was rinsed with EtOAc (2 × 80 mL), and filtrate was concentrated under reduced pressure. Then, oily residue was diluted with EtOAc (400 mL), washed with water/brine (250 mL, 1/1), and separated. The organic layer was washed with brine (50 mL), dried over $MgSO_4$, filtered, and concentrated under reduced pressure. The crude material was purified

https://doi.org/10.1021/acs.jmedchem.4c02225
J. Med. Chem. 2025, 68, 2981−3003

Scheme 5. Medicinal Chemistry Route to EP652[a]

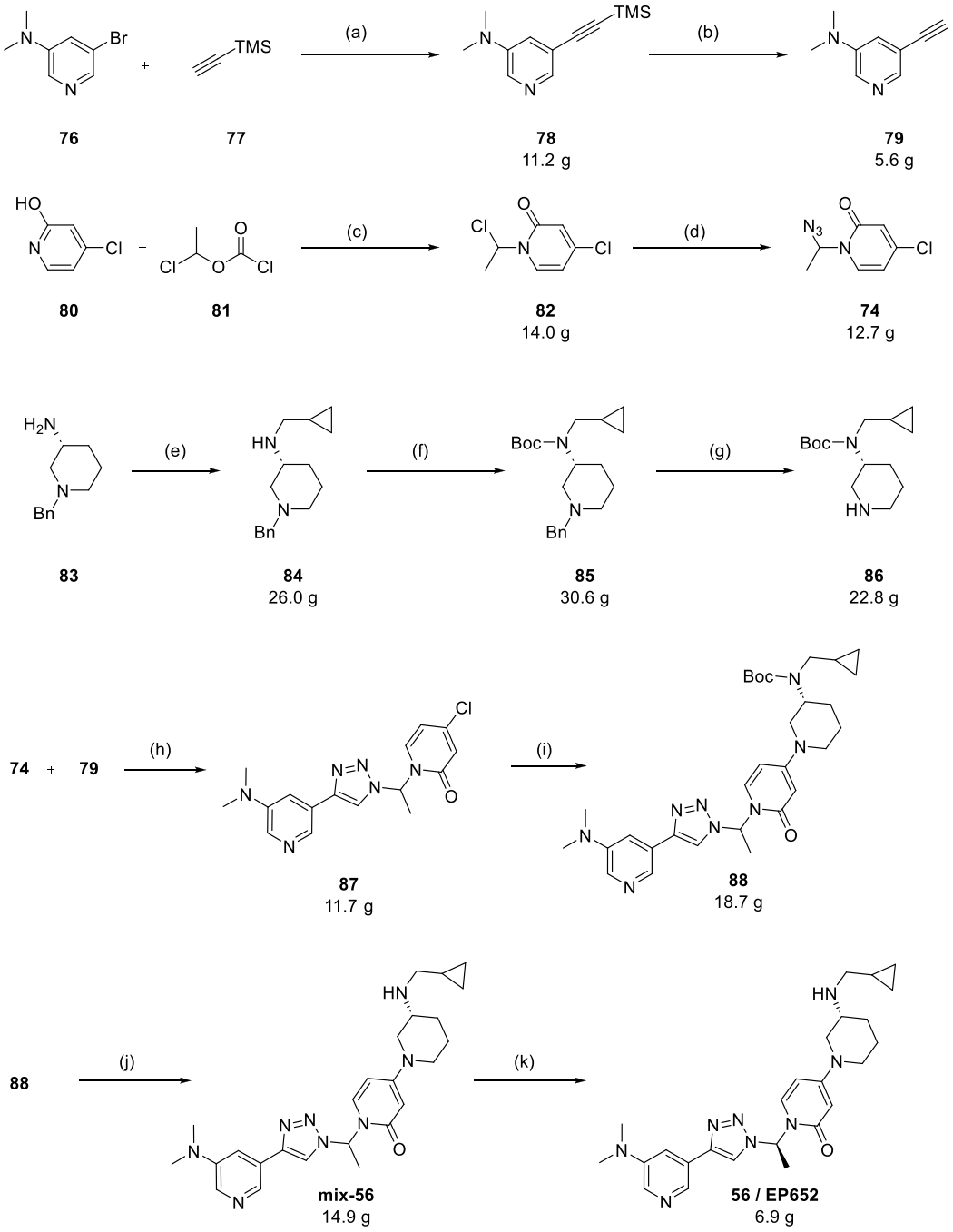

[a]Reagents and conditions: (a) CuI, TPP_2PdCl_2, TPP, TEA, THF, 65 °C, 98%; (b) K_2CO_3, MeOH, RT, 74%; (c) DABCO, DCE/DMF, 60 °C, 87%; (d) NaN_3, DMF, RT, 95%; (e) *c*PrCHO, $NaBH_4$, $Ti(OiPr)_4$, MeOH, 0 °C to RT, 90%; (f) Boc_2O, TEA, DCM, 0 °C to RT, 93%; (g) Pd/C, $NH_2NH_2{\cdot}H_2O$, EtOH, 80 °C, 100%; (h) CuI, DMF, RT, 89%; (i) **86**, TEA, NMP, 120 °C, 93%; (j) HCl 4 M, MeOH, RT, 94%; (k) Chiral preparative HPLC separation, 47%.

by an automated flash chromatography system (dry load with Celite, 0 to 50% EtOAc in heptane) to afford intermediate **78** (11.24 g, 98% yield, 100% purity (method B)) as a gray solid. *m*/*z* (ES^+): $[M + H]^+$ = 219. ^1H NMR (300 MHz, $CDCl_3$) δ 8.05 (s, 2H), 7.01 (dd, *J* = 3.0, 1.7 Hz, 1H), 2.97 (s, 6H), 0.26 (s, 9H). ^{13}C NMR (75.5 MHz, $CDCl_3$) δ: 145.5, 140.8, 134.7, 121.2, 119.8, 102.9, 96.7, 40.1, 0.1. TLC (hept/EtOAc, 1/1, v/v, UV 254 nm): $R_f \sim 0.50$.

*5-Ethynyl-N,N-dimethylpyridin-3-amine (**79**).* To a solution of **78** (11.24 g, 51.47 mmol) in anhydrous methanol (300 mL) was added potassium carbonate (1.80 g, 12.89 mmol). The reaction mixture was stirred at RT for 10 min, and then filtered on a Celite pad, and the resulting filtrate was concentrated under reduced pressure. The crude material was purified by an automated flash chromatography system (dry load with Celite, 0 to 40% EtOAc in heptane) to afford **79** (5.60 g, 74% yield, 100% purity (method B)) as a white solid. *m*/*z* (ES^+): $[M + H]^+$ = 147. ^1H NMR (300 MHz, $CDCl_3$) δ 8.09 (d, *J* = 3.0 Hz, 1H), 8.07 (d, *J* = 1.7 Hz, 1H), 7.03 (dd, *J* = 3.0, 1.7 Hz, 1H), 3.12 (s, 1H), 2.97 (s, 6H). ^{13}C NMR (75.5 MHz, $CDCl_3$) δ: 145.5, 140.8, 135.0, 121.3, 118.8, 81.6, 79.2, 40.1. TLC (hept/EtOAc, 1/1, v/v, UV 254 nm): $R_f \sim 0.15$.

*4-Chloro-1-(1-chloroethyl)pyridin-2(1H)-one (**82**).* To a suspension of 4-chloro-2-hydroxypyridine **80** (10 g, 74.88 mmol) in

https://doi.org/10.1021/acs.jmedchem.4c02225
J. Med. Chem. 2025, 68, 2981−3003

anhydrous DCE (250 mL) and DMF (16 mL) was added DABCO (4.25 g, 37.51 mmol) at RT. To the slurry was added 1-chloroethylchloroformate **81** (12.50 mL, 112.24 mmol) over 20 min at RT. The resulting mixture (beige suspension) was stirred at 60 °C under argon for 20 h. Because of incomplete conversion by HPLC-MS, a second addition of **80** (6 mL, 53.88 mmol) was carried out at RT, and the mixture was further stirred at 60 °C for 6.5 h. The reaction mixture was then cooled to RT and DCM (400 mL) was added. The suspension was filtered, and solid was rinsed with DCM (40 mL). The filtrate was washed with water (400 mL), saturated aqueous $NaHCO_3$ (400 mL), and brine (10 mL), dried over $MgSO_4$, filtered, and concentrated under high vacuum to afford crude intermediate **82** (13.97 g, 87% yield, 90% purity (method B)) as orange oil. m/z (ES^+): $[M + H]^+$ = 192, 194. ^1H NMR (300 MHz, $CDCl_3$) δ 7.48 (d, J = 7.5 Hz, 1H), 6.96 (q, J = 6.6 Hz, 1H), 6.57 (d, J = 2.3 Hz, 1H), 6.29 (dd, J = 6.6, 2.3 Hz, 1H), 1.87 (d, J = 6.6 Hz, 3H). ^{13}C NMR (75.5 MHz, $CDCl_3$) δ: 160.1, 147.4, 132.6, 119.5, 109.4, 63.4, 25.7.

*1-(1-Azidoethyl)-4-chloropyridin-2(1H)-one (**74**).* **82** (13.94 g, 65.33 mmol) was suspended in anhydrous DMF (100 mL), and sodium azide (5.60 g, 85.28 mmol) was added. The reaction mixture was stirred at RT under argon for 1 h. The mixture was then diluted with water (400 mL) and extracted with EtOAc (5 × 100 mL). The combined organic layers were washed with water (6 × 100 mL), brine (100 mL), dried over $MgSO_4$, filtered, and concentrated under reduced pressure to afford crude intermediate **74** (12.69 g, 95% yield, 97% purity (method A)) as orange oil. m/z (ES^+): $[M + H]^+$ = 199, 201. ^1H NMR (300 MHz, $CDCl_3$) δ 7.49 (d, J = 7.6 Hz, 1H), 6.98 (q, J = 6.6 Hz, 1H), 6.59 (d, J = 2.3 Hz, 1H), 6.30 (dd, J = 7.7, 2.3 Hz, 1H), 1.88 (d, J = 6.6 Hz, 3H). ^{13}C NMR (75.5 MHz, $CDCl_3$) δ: 160.1, 147.4, 132.6, 119.5, 109.4, 92.5, 63.4, 29.8, 25.7.

*(R)-1-Benzyl-N-(cyclopropylmethyl)piperidin-3-amine (**84**).* To a solution of cyclopropanecarboxaldehyde (9 mL, 116.83 mmol) in anhydrous methanol (80 mL) under an argon atmosphere at 0 °C was added titanium(IV) isopropoxide (60 mL, 196.58 mmol) over 10 min to afford a white milky suspension, which was stirred at 0 °C for 30 min. Then, a solution of (*R*)-1-benzylpiperidin-3-amine **83** (19.95 g, 104.85 mmol) in anhydrous methanol (30 mL) was added over 10 min. The resulting light yellow milky suspension was stirred at 0 °C for 15 min and then 2 h at RT. The reaction mixture was cooled to 0 °C, and sodium borohydride (9 g, 237.89 mmol) was added portion-wise over 40 min; then, stirring was continued at 0 °C for 5 min and then 1.5 h at RT. MeOH (100 mL) and 2.8% aqueous NH_4OH solution (250 mL) were added at RT to the mixture, and the suspension was stirred at RT for 16 h and then filtered through Celite (1 cm thick), and the solid was rinsed with MeOH (2 × 200 mL). Methanol was removed under reduced pressure to afford a biphasic yellow oil. Water (60 mL) was added, and organics were extracted with DCM (3 × 200 mL). The combined organic layers were washed with water (250 mL) and brine (250 mL), and then dried over $MgSO_4$, filtered through cotton wool, and concentrated under reduced pressure to afford crude intermediate **84** (25.98 g, 90% yield, 89% purity (method B)) as light brown oil. m/z (ES^+): $[M + H]^+$ = 245. ^1H NMR (300 MHz, $CDCl_3$) δ 7.36−7.18 (m, 5H), 3.50 (s, 2H), 2.83−2.54 (m, 3H), 2.43 (qd, J = 11.8, 6.8 Hz, 2H), 2.10 (td, J = 10.4, 3.2 Hz, 1H), 1.96 (dd, J = 10.6, 8.2 Hz, 1H), 1.88−1.75 (m, 1H), 1.76−1.09 (m, 5H), 1.01−0.82 (m, 1H), 0.50−0.41 (m, 2H), 0.12−0.02 (m, 2H). ^{13}C NMR (75.5 MHz, CD_3OD) δ: 138.8, 130.7, 129.3, 128.3, 64.3, 59.3, 54.9, 54.8, 52.7, 31.2, 24.5, 11.6, 4.0 (2C).

*tert-Butyl (R)-(1-Benzylpiperidin-3-yl)(cyclopropylmethyl)-carbamate (**85**).* To an orange solution of crude **84** (25.88 g, 94.25 mmol) in anhydrous DCM (350 mL) under an argon atmosphere at 0 °C was added triethylamine (27 mL, 191.78 mmol), followed by a solution of di-*tert*-butyldicarbonate (24.8 g, 113.63 mmol) in anhydrous DCM (50 mL) over 10 min, to afford an orange solution, which was stirred at RT for 16 h. A solution of 2-aminoethanesulfonic acid (9.70 g, 75.96 mmol) in a 2 M aqueous solution of NaOH (280 mL, 560 mmol) was added (to quench the excess of Boc_2O) at RT, and the reaction mixture was stirred at RT for 30 min. Water (100 mL) was added, and layers were separated. The aqueous layer was further extracted with DCM (300 mL), and the combined organic layers were washed with NaOH 1 M (200 mL), and then water (200 mL) and brine (200 mL). The organic layer was dried over $MgSO_4$ and filtered through cotton wool, and the filtrate was concentrated under reduced pressure to afford crude intermediate **85** (38.2 g) as a light-brown oil. The crude material was purified by an automated flash chromatography system (dry load with 50 g of silica, 0 to 25% EtOAc in heptane) to afford intermediate **85** (30.6 g, 93% yield, 99% purity (method B)) as a colorless oil. m/z (ES^+): $[M + H]^+$ = 345. ^1H NMR (300 MHz, CD_3OD) δ 7.37−7.19 (m, 5H), 3.79 (bs, 1H), 3.61 (d, J = 12.9 Hz, 1H), 3.48 (d, J = 12.9 Hz, 1H), 3.15−2.95 (m, 2H), 2.91−2.80 (m, 2H), 2.15 (t, J = 10.8 Hz, 1H), 1.94 (td, J = 11.5, 2.9 Hz, 1H), 1.83−1.72 (m, 2H), 1.72−1.58 (m, 2H), 1.41 (s, 9H), 1.01−0.83 (m, 1H), 0.53−0.36 (m, 2H), 0.30−0.15 (m, 2H). ^{13}C NMR (75.5 MHz, CD_3OD) δ 157.2, 138.6, 130.6, 129.3, 128.3, 80.9, 64.1, 58.0, 55.5, 54.3, 50.1, 33.0, 29.7, 28.8, 25.8, 23.7, 14.4, 12.6, 4.7, 4.4. TLC (hept/EtOAc, 4/1, v/v, UV 254 nm): $R_f \sim 0.40$.

*tert-Butyl (R)-(Cyclopropylmethyl)(piperidin-3-yl)carbamate (**86**).* A solution of **85** (30.6 g, 87.94 mmol) in anhydrous ethanol (350 mL) was degassed by argon bubbling. 10% palladium on activated carbon (9.3 g, 8.74 mmol) was added under an argon atmosphere, followed by hydrazine monohydrate (8.60 mL, 173.74 mmol) dropwise over 30 s, and the reaction mixture was stirred at 80 °C for 1.25 h. The reaction mixture was cooled to RT and then filtered through a short pad of Celite, which was rinsed with MeOH (2 × 200 mL) and DCM (2 × 200 mL). The filtrate was concentrated under reduced pressure. The residue was diluted with DCM (200 mL) and concentrated under reduced pressure to afford crude intermediate **86** (22.8 g, 100% yield, 98% purity (method B)) as a colorless oil. m/z (ES^+): $[M + H]^+$ = 255. ^1H NMR (300 MHz, $CDCl_3$) δ 3.65 (bs, 1H), 3.15−2.92 (m, 4H), 2.79 (t, J = 11.4 Hz, 1H), 2.46 (td, J = 12.5, 2.7 Hz, 1H), 2.05 (s, 1H), 1.94−1.83 (m, 1H), 1.83−1.65 (m, 2H), 1.61−1.49 (m, 1H), 1.46 (s, 9H), 1.03−0.85 (m, 1H), 0.54−0.40 (m, 2H), 0.29−0.18 (m, 2H). ^{13}C NMR (75.5 MHz, CD_3OD) δ 157.1, 81.0, 56.5, 50.4, 46.4 (2C), 30.3, 28.8, 27.7, 12.6, 4.7, 4.4.

*4-Chloro-1-(1-(4-(5-(dimethylamino)pyridin-3-yl)-1H-1,2,3-triazol-1-yl)ethyl)pyridin-2(1H)-one (**87**).* Copper(I) iodide (147 mg, 0.77 mmol) was added to a solution of **74** (8.4 g, 40.18 mmol) and **79** (5.6 g, 38.31 mmol) in anhydrous DMF (38 mL, previously degassed by argon bubbling for 10 min) under an argon atmosphere to afford a yellow solution, which was stirred at RT in the dark. After 1 h, the mixture was diluted with saturated aqueous $NaHCO_3$ (200 mL) and extracted with EtOAc (2 × 200 mL). Organic layers were merged, washed with brine (2 × 100 mL), 3 wt % NH_4OH (2 × 250 mL, then 5 × 50 mL), and brine (50 mL), dried over $MgSO_4$, filtered, and concentrated under reduced pressure to afford intermediate **87** (11.73 g, 89% yield, 100% purity (method B)) as a white solid. m/z (ES^+): $[M + H]^+$ = 347, 347. ^1H NMR (300 MHz, $CDCl_3$) δ 8.30 (s, 1H), 8.11 (s, 1H), 8.07 (s, 1H), 7.60 (d, J = 7.6 Hz, 1H), 7.52 (q, J = 7.0 Hz, 1H), 7.48−7.43 (m, 1H), 6.62 (d, J = 2.3 Hz, 1H), 6.26 (dd, J = 7.6, 2.3 Hz, 1H), 3.02 (s, 6H), 2.20 (d, J = 7.0 Hz, 3H). ^{13}C NMR (75.5 MHz, $CDCl_3$) δ: 160.7, 148.0, 146.1, 135.1, 132.8, 121.0, 119.6, 115.4, 63.1, 40.2, 19.0. TLC (DCM/MeOH, 95/5, v/v, UV 254 nm): $R_f \sim 0.20$.

*tert-Butyl (Cyclopropylmethyl)((3R)-1-(1-(1-(4-(5-(dimethylamino)pyridin-3-yl)-1H-1,2,3-triazol-1-yl)ethyl)-2-oxo-1,2-dihydropyridin-4-yl)piperidin-3-yl)carbamate (**88**).* To a solution of intermediate **87** (11.63 g, 33.73 mmol) and intermediate **86** (9.65 g, 37.18 mmol) in anhydrous NMP (34 mL) under an argon atmosphere at RT was added triethylamine (9.7 mL, 69.59 mmol), and the mixture was stirred at 120 °C for 16 h. The reaction mixture was then cooled to RT, diluted with EtOAc (150 mL), and washed with water (5 × 30 mL) and brine (3 × 30 mL). The organic layer was dried over $MgSO_4$, filtered, and concentrated under reduced pressure to afford a crude brown solid. The crude material was purified by an automated flash chromatography system (loaded in DCM (50 mL), 0 to 9.5% MeOH in DCM) to afford intermediate **88** (18.67 g, 93% yield, 95% purity (method A)) as an off-white solid. m/z (ES^+): $[M + H]^+$ = 563. ^1H NMR (300 MHz, $CDCl_3$) δ 8.32 (d, J =

https://doi.org/10.1021/acs.jmedchem.4c02225
J. Med. Chem. 2025, 68, 2981−3003

1.7 Hz, 1H), 8.15−8.04 (m, 2H), 7.59−7.50 (m, 1H), 7.46 (dd, J = 2.4 Hz, 1H), 7.42 (d, J = 8.1 Hz, 1H), 6.00 (dd, J = 8.7, 2.5 Hz, 1H), 5.66 (d, J = 2.8 Hz, 1H), 3.76 (t, J = 13.1 Hz, 2H), 3.62−3.49 (m, 1H), 3.24−3.03 (m, 3H), 3.01 (s, 6H), 2.76 (t, J = 12.9 Hz, 1H), 2.15 (d, J = 7.0 Hz, 3H), 2.02−1.84 (m, 2H), 1.84−1.72 (m, 1H), 1.69−1.51 (m, 1H), 1.46 (s, 9H), 0.92 (p, J = 6.8 Hz, 1H), 0.55−0.43 (m, 2H), 0.28−0.16 (m, 2H). ^{13}C NMR (75.5 MHz, $CDCl_3$) δ: 162.73, 156.53, 155.34, 155.30, 146.30, 145.72, 135.37, 134.99, 132.16, 126.18, 121.03, 115.48, 99.25, 94.49, 94.46, 80.16, 62.29, 54.10, 53.96, 50.86, 50.52, 50.19, 50.06, 46.88, 40.25, 28.64, 24.60, 24.58, 18.68, 11.85, 4.36, 4.33, 4.02. ^{13}C NMR (75.5 MHz, $CDCl_3$) δ: 162.7, 156.5, 155.3, 155.3, 146.3, 145.7, 135.4, 135.0, 132.2, 126.2, 121.0, 115.5, 99.3, 94.5, 94.5, 80.2, 62.3, 54.1, 54.0, 50.9, 50.5, 50.2, 50.1, 46.9, 40.3, 28.6, 24.6, 24.6, 18.7, 11.9, 4.4, 4.3, 4.0. TLC (DCM/MeOH, 95/5, v/v, UV 254 nm): R_f ∼ 0.20.

*4-((R)-3-((CycloPropylmethyl)amino)piperidin-1-yl)-1-(1-(4-(5-(dimethylamino)pyridin-3-yl)-1H-1,2,3-triazol-1-yl)ethyl)pyridin-2(1H)-one (**mix-56**).* To a mixture of intermediate **88** (19.67 g, 33.21 mmol) in anhydrous methanol (170 mL) under an argon atmosphere at RT was added hydrogen chloride 4 M in 1,4-dioxane (200 mL, 800 mmol), and resulting yellow solution was stirred at RT for 20 min. The reaction mixture was then concentrated under reduced pressure to afford a brown paste, which was solubilized in water (350 mL), basified with K_2CO_3 solid (pH ∼ 11), and extracted with EtOAc (3 × 200 mL) and EtOAc/MeOH (95/5, 4 × 250 mL). Organic layers were merged, washed with brine (50 mL), dried over $MgSO_4$, filtered, concentrated under reduced pressure, and dried under high vacuum for 1.5 h to afford **mix-56** (14.92 g, 94% yield, 97% purity (method A)) as an off-white solid. m/z (ES^+): $[M + H]^+$ = 463.

*4-((R)-3-((Cyclopropylmethyl)amino)piperidin-1-yl)-1-((R)-1-(4-(5-(dimethylamino)pyridin-3-yl)-1H-1,2,3-triazol-1-yl)ethyl)pyridin-2(1H)-one (**56/EP652**).* The separation of the two diastereomers of **mix-56** (14.9 g) was performed by chiral preparative HPLC (column: Chiralpak IA 5 μm, 20 mm × 250 mm, mobile phase: TBME/MeOH/DCM/DEA 40/40/20/0.1, flow rate: 20 mL/min, injection volume: 1 mL (40 mL of the mobile phase used to dissolve **mix-56**)). The second peak was collected (t_R = 10.1 min) and fractions concentrated under reduced pressure to afford **56** (6.85 g, 47% yield, 99% purity (method A)) as an off-white solid. m/z (ES^+): $[M + H]^+$ = 463. Chiral HPLC: de = 99.9% (column: Chiralpak IA 5 μm, 4.6 mm × 250 mm, mobile phase: TBME/MeOH/DCM/DEA 40/40/20/0.1, flow rate: 1 mL/min, t_R = 5.4 and 7.7 min). ^{1}H NMR (300 MHz, $CDCl_3$) δ 8.24 (d, J = 1.7 Hz, 1H), 8.06 (s, 1H), 7.99 (d, J = 2.9 Hz, 1H), 7.46 (q, J = 7.0 Hz, 1H), 7.39−7.31 (m, 2H), 5.90 (dd, J = 8.1, 2.8 Hz, 1H), 5.56 (d, J = 2.8 Hz, 1H), 3.72−3.61 (m, 1H), 3.58−3.44 (m, 1H), 2.91 (s, 6H), 2.83 (ddd, J = 13.2, 11.0, 3.0 Hz, 1H), 2.64 (dd, J = 12.6, 9.3 Hz, 1H), 2.59−2.49 (m, 1H), 2.47−2.32 (m, 2H), 2.07 (d, J = 7.0 Hz, 3H), 1.94−1.82 (m, 1H), 1.69−1.59 (m, 1H), 1.50−1.35 (m, 1H), 1.33−1.18 (m, 1H), 0.89−0.71 (m, 1H), 0.45−0.29 (m, 2H), 0.08 − −0.06 (m, 2H), 1H exchanged with solvent. ^{13}C NMR (75.5 MHz, $CDCl_3$) δ: 162.5, 156.5, 146.1, 145.4, 135.1, 134.7, 131.9, 126.0, 120.9, 115.2, 99.0, 93.9, 62.1, 53.2, 52.3, 52.3, 47.0, 40.0 (2C), 31.4, 23.1, 18.4, 11.4, 3.4, 3.3. HRMS (ES^+) calculated for $C_{25}H_{34}KN_8O$ $[M + K]^+$ = 501.2487, found 501.2481.

■ ASSOCIATED CONTENT

Supporting Information

The Supporting Information is available free of charge at https://pubs.acs.org/doi/10.1021/acs.jmedchem.4c02225.

Experimental procedures for all compounds and NMR spectra; SPA, ATPlite, spheroid, and intracellular m^{6}A assays; plasma protein binding determination; plasma pharmacokinetic studies in rats and mice; biomarker evaluation by Western blots; full description of *in vivo* cancer models; method for LogD determination; and cocrystallization details: protein production, crystallization of *apo* complex, and tabulated parameters of data collection and structure refinement for compounds **31**, **56** (**EP652**), and **59** (PDF)

Molecular formula strings (CSV)

Accession Codes

Crystallographic structures of **31**, **56** (**EP652**), and **59** complexed to truncated METTL3/14 proteins been deposited at the Protein Data Bank with the accession codes 9G4U, 9G4S, and 9G4W, respectively. The authors will release the atomic coordinates and experimental data upon article publication.

■ AUTHOR INFORMATION

Corresponding Author

Guillaume Dutheuil − *Epics Therapeutics SA, Gosselies 6041, Belgium*; orcid.org/0000-0002-8887-4823; Email: gdutheuil@epicstx.com

Authors

Killian Oukoloff − *Epics Therapeutics SA, Gosselies 6041, Belgium*

Julien Korac − *Epics Therapeutics SA, Gosselies 6041, Belgium*

François Lenoir − *Epics Therapeutics SA, Gosselies 6041, Belgium*

Mohamed El Bousmaqui − *Epics Therapeutics SA, Gosselies 6041, Belgium*

Nicolas Probst − *Epics Therapeutics SA, Gosselies 6041, Belgium*; orcid.org/0000-0003-1941-7132

Alexey Lapin − *Epics Therapeutics SA, Gosselies 6041, Belgium*

Galina Nakhabina − *Epics Therapeutics SA, Gosselies 6041, Belgium*

Catherine Sorlet − *Epics Therapeutics SA, Gosselies 6041, Belgium*

Nicolas Parmentier − *Epics Therapeutics SA, Gosselies 6041, Belgium*; orcid.org/0000-0002-9114-3976

Delphine Karila − *Paraza Pharma, Inc., Montréal H4S 2E1, Canada*

Nugzar Ghavtadze − *Paraza Pharma, Inc., Montréal H4S 2E1, Canada*

Paméla Casault − *Paraza Pharma, Inc., Montréal H4S 2E1, Canada*; orcid.org/0000-0002-4500-7180

Stephen Claridge − *Paraza Pharma, Inc., Montréal H4S 2E1, Canada*

Selma Sapmaz − *Cresset Biomolecular Discovery Limited, Litlington SG8 0SS, United Kingdom*

Martin J. Slater − *Cresset Biomolecular Discovery Limited, Litlington SG8 0SS, United Kingdom*

Graeme L. Fraser − *Epics Therapeutics SA, Gosselies 6041, Belgium*

Complete contact information is available at: https://pubs.acs.org/10.1021/acs.jmedchem.4c02225

Author Contributions

The manuscript was written through contributions of all authors. All authors have given approval to the final version of the manuscript.

Funding

The work was mainly funded by Epics Therapeutics. This research project was partially supported by a research grant from the Walloon Region, Belgium.

Notes

All animal experiments performed in the manuscript were conducted in compliance with institutional guidelines.
The authors declare no competing financial interest.

■ ACKNOWLEDGMENTS

We thank our colleagues in the *in vitro* and *in vivo* profiling teams, as well as the pharmacology team for conducting studies in support of this work. We are grateful as well to Dr. Dawidowski and his team at Selvita, Krakow, Poland, for determination of X-ray structures of truncated human METTL3/14 complex with our compounds. Finally, we are grateful to Dr. Slater and his team at Cresset Discovery, UK, for the exceptional modeling work conducted.

■ ABBREVIATIONS

ADME, absorption, distribution, metabolism, and excretion; ADMP, 2-azido-1,3-dimethylimidazolinium hexafluorophosphate; Alk, alkyl; ALIS, Automated Ligand Identification System; AML, acute myeloid leukemia; Ar, argon; ASMS, affinity selection-mass spectrometry; ATP, adenosine triphosphate; AUC, aera under the curve; AUC_u, unbound aera under the curve; BLI, bioluminescence imaging; Boc, *tert*-butyl carbonate; Boc_2O, di-*tert*-butyl dicarbonate; *c*Bu, cyclobutyl; $CDCl_3$, deuterated chloroform; CDX, cell line-derived xenograft; Cl, clearance; Cl_u, unbound clearance; *c*Pr, cyclopropyl; ctl, control; CYP, cytochrome P450; DABCO, 1,4-diazabicyclo[2.2.2]octane; DCE, dichloroethane; DCM, dichloromethane; *de*, diastereomeric excess; DEA, diethylamine; DMF, *N*,*N*-dimethylformamide; DPPA, diphenyl phosphoryl azide; DRC, dose−response curve; DSC, differential scanning calorimetry; EC, electrostatic complementarity; ES^+, electrospray positive ionization; EtOAc, ethyl acetate; EtOH, ethanol; EWG, electron-withdrawing group; FG, functional group; FTO, fat mass and obesity-associated; hept, heptane; hERG, human Ether-à-go-go-related gene; HLM, human liver microsomes; HPLC, high-performance liquid chromatography; HTS, high-throughput screening; Hz, hertz; IC_{50}, half-maximum inhibitory concentration; ip, intraperitoneal administration; iv, intravenous administration; *J*, coupling constant; LLE, ligand lipophilic efficiency; MeOH, methanol; METTL3, methyltransferase-like 3; mfu, mouse fraction unbound (PPB); MS, mass spectrometry; MsCl, mesyl chloride; MSMS, tandem mass spectrometry; MW, molecular weight; NMP, 1-methyl-2-pyrrolidone; NMR, nuclear magnetic resonance; NSCLC, nonsmall cancer lung cell; PAINS, pan-assay interference compounds; PDB, Protein Data Bank; PDX, patient-derived xenograft; PK, pharmacokinetic; PPB, plasma protein binding; PROTAC, proteolysis-targeting chimera; QD, quaque die (once a day); QED, quantitative estimate of drug-likeness; QSAR, quantitative structure−activity relationship; R_f, retention factor; rfu, rat fraction unbound (PPB); RLM, rat liver microsomes; RNA, ribonucleic acid; RT, room temperature; SAM, *S*-adenosylmethionine; SAR, structure−activity relationship; SBDD, structure-based drug design; S_NAr, aromatic nucleophilic substitution; SPA, scintillation proximity assay; SPR, surface plasma resonance; TBME, *tert*-butyl methyl ether; TEA, triethylamine; TFA, trifluoroacetic acid; TGA, thermogravimetric analysis; THF, tetrahydrofuran; TLC, thin-layer chromatography; TMS, trimethylsilyl; TPP, triphenylphosphine; TPSA, topologic polar surface area; UV, ultraviolet; VS, virtual screening

■ REFERENCES

(1) Roundtree, I. A.; Evans, M. E.; Pan, T.; He, C. Dynamic RNA modifications in gene expression regulation. *Cell* **2017**, *169*, 1187−1200. Meyer, K. D.; Saletore, Y.; Zumbo, P.; Elemento, O.; Mason, C. E.; Jaffrey, S. R. Comprehensive analysis of mRNA methylation reveals enrichment in 3' UTRs and near stop codons. *Cell* **2017**, *149*, 1635−1646. Liu, J.; Yue, Y.; Han, D.; Wang, X.; Fu, Y.; Zhang, L.; Jia, G.; Yu, M.; Lu, Z.; Deng, X.; Dai, Q.; Chen, W.; He, C. A METTL3-METTL14 complex mediates mammalian nuclear RNA N6-adenosine methylation. *Nat. Chem. Biol.* **2014**, *10*, 93−95.

(2) Zaccara, S.; Ries, R. J.; Jaffrey, S. R. Reading, writing and erasing mRNA methylation. *Nat. Rev. Mol. Cell Biol.* **2019**, *20*, 608−624.

(3) Wang, X.; Feng, J.; Xue, Y.; Guan, Z.; Zhang, D.; Liu, Z.; Gong, Z.; Wang, Q.; Huang, J.; Tang, C.; Zou, T.; Yin, P. Structural basis of N(6)-adenosine methylation by the METTL3-METTL14 complex. *Nature* **2016**, *534*, 575−578.

(4) Garcias Morales, D.; Reyes, J. L. A birds'-eye view of the activity and specificity of the mRNA m^6A methyltransferase complex. *Wiley Interdiscip. Rev.: RNA* **2021**, *12*, No. e1618. Knuckles, P.; Lence, T.; Haussmann, I. U.; Jacob, D.; Kreim, N.; Carl, S. H.; Masiello, I.; Hares, T.; Villaseñor, R.; Hess, D.; Andrade-Navarro, M. A.; Biggiogera, M.; Helm, M.; Soller, M.; Bühler, M.; Roignant, J.-Y. Zc3h13/Flacc is required for adenosine methylation by bridging the mRNA-binding factor Rbm15/Spenito to the m^6A machinery component Wtap/Fl(2)d. *Genes Dev.* **2018**, *32*, 415−429.

(5) Xu, P.; Ge, R. Roles and drug development of METTL3 (methyltransferase-like 3) in anti-tumor therapy. *Eur. J. Med. Chem.* **2022**, *230*, 114118−114141. Cai, Y.; Feng, R.; Lu, T.; Chen, X.; Zhou, X.; Wang, X. Novel insights into the m^6A-RNA methyltransferase METTL3 in cancer. *Biomarker Res.* **2021**, *9*, 27.

(6) Vu, L. P.; Pickering, B. F.; Cheng, Y.; Zaccara, S.; Nguyen, D.; Minuesa, G.; Chou, T.; Chow, A.; Saletore, Y.; MacKay, M.; Schulman, J.; Famulare, C.; Patel, M.; Klimek, V. M.; Garrett-Bakelman, F. E.; Melnick, A.; Carroll, M.; Mason, C. E.; Jaffrey, S. R.; Kharas, M. G. The N6-methyladenosine (m^6A)-forming enzyme METTL3 controls myeloid differentiation of normal hematopoietic and leukemia cells. *Nat. Med.* **2017**, *23*, 1369−1376. Zhang, Y.; Liu, S.; Zhao, T.; Dang, C. METTL3-mediated m^6A modification of Bcl-2 mRNA promotes non-small cell lung cancer progression. *Oncol. Rep.* **2021**, *46* (2), 163−172.

(7) Oerum, S.; Catala, M.; Atdjian, C.; Brachet, F.; Ponchon, L.; Barraud, P.; Iannazzo, L.; Droogmans, L.; Braud, E.; Ethève-Quelquejeu, M.; Tisné, C. Bisubstrate analogues as structural tools to investigate m^6A methyltransferase active sites. *RNA Biol.* **2019**, *16*, 798−808. Ye, F.; Zhang, W.; Lu, W.; Xie, Y.; Jiang, H.; Jin, J.; Luo, C. Identification of novel inhibitors against coactivator associated arginine methyltransferase 1 based on virtual screening and biological assays. *BioMed Res. Int.* **2016**, 1−8.

(8) Moroz-Omori, E. V.; Huang, D.; Kumar Bedi, R.; Cheriyamkunnel, S. J.; Bochenkova, E.; Dolbois, A.; Rzeczkowski, M. D.; Li, Y.; Wiedmer, L.; Caflisch, A. METTL3 inhibitors for epitranscriptomic modulation of cellular processes. *ChemMedChem* **2021**, *16*, 3035.

(9) Yankova, E.; Blackaby, W.; Albertella, M.; Rak, J.; De Braekeleer, E.; Tsagkogeorga, E.; Pilka, E. S.; Aspris, D.; Leggate, D.; Hendrick, A. G.; Webster, N. A.; Andrews, B.; Fosbeary, R.; Guest, P.; Irigoyen, N.; Eleftheriou, M.; Gozdecka, M.; Dias, J. M. L.; Bannister, A. J.; Vick, B.; Jeremias, I.; Vassiliou, G. S.; Rausch, O.; Tzelepis, K.; Kouzarides, K. Small molecule inhibition of METTL3 as a strategy against myeloid leukaemia. *Nature* **2021**, *593*, 597−601.

(10) Fiorentino, F.; Menna, M.; Rotili, D.; Valente, S.; Mai, A. METTL3 from Target Validation to the First Small-Molecule Inhibitors: A Medicinal Chemistry Journey. *J. Med. Chem.* **2023**, *66* (3), 1654−1677. Li, H.; Zhang, Q.; Feng, Q.; You, Q.; Guo, X. The development of small molecules targeting methyltransferase-like 3. *Drug Discovery Today* **2023**, *28* (4), No. 103513.

(11) Bedi, R. K.; Huang, D.; Eberle, S. A.; Wiedmer, L.; Śledź, P.; Caflisch, A. Small-molecule inhibitors of METTL3, the major human epitranscriptomic writer. *ChemMedChem.* **2020**, *15* (9), 744−748.

https://doi.org/10.1021/acs.jmedchem.4c02225
J. Med. Chem. 2025, 68, 2981−3003

(12) Bedi, R. K.; Huang, D.; Li, Y.; Caflisch, A. Structure-based design of inhibitors of the m^{6}A-RNA writer enzyme METTL3. *ACS Bio. Med. Chem. Au* **2023**, *3* (4), 359−370.
(13) Dolbois, A.; Bedi, R. K.; Bochenkova, E.; Müller, A.; Moroz-Omori, E. V.; Huang, D.; Caflisch, A. 1,4,9-Triazaspiro[5.5]undecan-2-one derivatives as potent and selective METTL3 inhibitors. *J. Med. Chem.* **2021**, *64* (17), 12738−12760.
(14) Guirguis, A. A.; Ofir-Rosenfeld, Y.; Knezevic, K.; Blackaby, W.; Hardick, D.; Chan, Y.; Motazedian, A.; Gillespie, A.; Vassiliadis, D.; Lam, E. E. N.; Tran, K.; Andrews, B.; Harbour, M. E.; Vasiliauskaite, L.; Saunders, C. J.; Tsagkogeorga, G.; Azevedo, A.; Obacz, J.; Pilka, E. S.; Carkill, M.; MacPherson, L.; Wainwright, E. N.; Liddicoat, B.; Blyth, B. J.; Albertella, M. R.; Rausch, O.; Dawson, M. A. Inhibition of METTL3 results in a cell-intrinsic interferon response that enhances antitumor immunity. *Cancer Discovery* **2023**, *13* (10), 2228−2247.
(15) Blackaby, W.; Hardick, D.; Thomas, E.; Bookfield, F. A.; Bubert, C.; Shepherd, J.; Ridgill, M. P. Preparation of imidazopyridines and related derivatives as MeTTL3 inhibitors. WO 2020/201773 A1, Oct 08, 2020. Blackaby, W.; Hardick, D.; Thomas, E.; Bookfield, F. A.; Shepherd, J.; Bubert, C.; Ridgill, M. P. Preparation of polyheterocyclic compounds as METTL3 inhibitors. WO 2021/111124 A1, Jun 10, 2021. Hardick, D.; Blackaby, W.; Thomas, E.; Bookfield, F. A.; Shepherd, J.; Bubert, C.; Ridgill, M. P. Preparation of heteroaromatic compounds as METTL3 inhibitory compounds. WO 2022/074379 A1, Apr 14, 2022. Hardick, D.; Blackaby, W.; Thomas, E.; Bookfield, F. A.; Shepherd, J.; Bubert, C.; Ridgill, M. P. Preparation of nucleosides as inhibitors of N6-adenosine-methyltransferase METTL3. WO 2022/074391 A1, Apr 14, 2022. Bubert, C.; Ridgill, M. P.; Canelli, T.; Hardick, D. Processes for the preparation of inhibitory compounds. WO 2022/254218 A1, Dec 08, 2022. Bayle, E. D.; Bucknell, S. J.; Thomas, E. J.; Hardick, D. J.; Harper, C.; Byrne, D.; Shepherd, J.; Ridgill, M. P.Inhibitory compounds. WO 2024/126897 A1, Dec 12 2024.
(16) https://www.stormtherapeutics.com/site/assets/files/1460/storm-asco-poster-72x42-may24-v5b_final.3w27wb.pdf.
(17) (a) Wynn, T. A.; Hodous, B. L.; Boriack-Sjodin, P. A.; Sickmier, E. A.; Mills, J. E. J.; Copeland, R. A. Preparation of nucleosides analogs as methyltransferase-like 3 (METTL3) modulators. WO 2021/079196, Apr 29, 2021. (b) Wynn, T. A.; Hodous, B. L.; Boriack-Sjodin, P. A.; Sickmier, E. A.; Mills, J. E. J.; Tasker, A. S.; Copeland, R. A. Preparation of substituted pyrrolopyrimidinamines as METTL3 modulators. WO 2021/081211 A1, Apr 29, 2021. (c) Daniels, M. H.; Wynn, T. A.; Sparling, B. A.; Sickmier, E. A.; Tasker, A. S. METTL3 modulators. WO 2022/081739 A1, Apr 21, 2022.
(18) Cheruvallath, Z. S.; Veal, J. M.; Stafford, J. A.; McBride, C. Preparation of 6,6-fused heterocyclic compounds as METTL3 inhibitors. WO 2023/129933 A2, Jul 07, 2023.
(19) Buker, S. M.; Gurard-Levin, Z. A.; Wheeler, B. D.; Scholle, M. D.; Case, A. W.; Hirsch, J. L.; Ribich, S.; Copeland, R. A.; Boriack-Sjodin, P. A. A mass spectrometric assay of METTL3/METTL14 methyltransferase activity. *SLAS Discovery* **2020**, *25* (4), 361−371. Annis, D. A.; Nickbarg, E.; Yang, X.; Ziebell, M. R.; Whitehurst, C. E. Affinity selection-mass spectrometry screening techniques for small molecule drug discovery. *Curr. Opin. Chem. Biol.* **2007**, *11*, 518−526.
(20) Very recently, an analogous approach was reported: Li, Z.; Feng, Y.; Han, H.; Jiang, X.; Chen, W.; Ma, Z.; Mei, Y.; Yuan, D.; Zhang, D.; Shi, J. A stapled peptide inhibitor targeting the binding interface of N6-adenosine-methyltransferase subunits METTL3 and METTL14 for cancer therapy. *Angew. Chem., Int. Ed.* **2024**, *63*, No. e202402611.
(21) *Work performed with our partner Cresset Discovery*: https://www.cresset-group.com/discovery/why-cresset-discovery/.
(22) (a) Miller, R. R.; Madeira, M.; Wood, H. B.; Geissler, W. M.; Raab, C. E.; Martin, I. J. Integrating the impact of lipophilicity on potency and pharmacokinetic parameters enables the use of diverse chemical space during small molecule drug optimization. *J. Med. Chem.* **2020**, *63* (21), 12156−12170. (b) Pennington, L. D.; Hesse, M. J.; Koester, D. C.; McAtee, R. C.; Qunies, A. A. M.; Xu, D. X. Property-Based Drug Design Merits a Nobel Prize. *J. Med. Chem.* **2024**, *67*, 11452−11458.
(23) (a) *Spark*; Cresset®: Litlington, Cambridgeshire, UK, https://www.cresset-group.com/software/spark/;. (b) Cheeseright, T.; Mackey, M.; Rose, S.; Vinter, A. Molecular field extrema as descriptors of biological activity: definition and validation. *J. Chem. Inf. Model.* **2006**, *46* (2), 665−676.
(24) *Lead Finder*; BioMolTech®: Toronto, Ontario, Canada, https://www.cresset-group.com/software/leadfinder.
(25) Bauer, M. R.; Mackey, M. D. Electrostatic complementarity as a fast and effective tool to optimize binding and selectivity of protein−ligand complexes. *J. Med. Chem.* **2019**, *62* (6), 3036−3050. *Flare*; Cresset®: Litlington, Cambridgeshire, UK, https://www.cresset-group.com/flare/.
(26) Śledź, P.; Jinek, M. Structural insights into the molecular mechanism of the m(6)A writer complex. *eLife* **2016**, *5*, No. e18434. Wang, P.; Doxtader, K. A.; Nam, Y. Structural Basis for Cooperative Function of Mettl3 and Mettl14 Methyltransferases. *Mol. Cell* **2016**, *63* (2), 306−317.
(27) Barbieri, I.; Tzelepis, K.; Pandolfini, L.; Shi, J.; Millán-Zambrano, G.; Robson, S. C.; Aspris, D.; Migliori, V.; Bannister, A. J.; Han, N.; De Braekeleer, E.; Ponstingl, H.; Hendrick, A.; Vakoc, C. R.; Vassiliou, G. S. Promoter-bound METTL3 maintains myeloid leukaemia by m^{6}A-dependent translation control. *Nature* **2017**, *552*, 126−131. Cheng, Y.; Luo, H.; Izzo, F.; Pickering, B. F.; Nguyen, D.; Myers, R.; Schurer, A.; Gourkanti, S.; Brüning, J. C.; Vu, L. P.; Jaffrey, S. R.; Landau, D. A.; Kharas, M. G. m^{6}A RNA methylation maintains hematopoietic stem cell identity and symmetric commitment. *Cell Reports* **2019**, *28* (7), 1703−1716. Pan, Z. P.; Wang, B.; Hou, D. Y.; You, R. L.; Wang, X. T.; Xie, W. H.; Huang, H. F. METTL3 mediates bone marrow mesenchymal stem cell adipogenesis to promote chemoresistance in acute myeloid leukaemia. *FEBS Open Bio.* **2021**, *11*, 1659−1672. Yankova, E.; Aspris, D.; Tzelepis, K. The N6-methyladenosine RNA modification in acute myeloid leukemia. *Curr. Opin. Hematol.* **2021**, *28* (2), 80−85. Sang, L.; Wu, X.; Yan, T.; Naren, D.; Liu, X.; Zheng, X.; Zhang, N.; Wang, H.; Li, Y.; Gong, Y. The m^{6}A RNA methyltransferase METTL3/METTL14 promotes leukemogenesis through the mdm2/p53 pathway in acute myeloid leukemia. *J. Cancer* **2022**, *13* (3), 1019−1030.
(28) Leeson, P. D.; Empfield, J. R. Reducing the risk of drug attrition associated with physicochemical properties. *Annu. Rep. Med. Chem.* **2010**, *45*, 381−391. and references therein
(29) Summerfield, S. G.; Yates, J. W. T.; Fairman, D. A. Free drug theory - No longer just a hypothesis? *Pharm. Res.* **2022**, *39* (2), 213−222. Trainor, G. L. The importance of plasma protein binding in drug discovery. *Expert Opin. Drug Discovery* **2007**, *2*, 51−64.
(30) Brameld, K. A.; Kuhn, B.; Reuter, D. C.; Stahl, M. Small molecule conformational preferences derived from crystal structure data. A medicinal chemistry focused analysis. *J. Chem. Inf. Model.* **2008**, *48*, 1−24.
(31) Poh, H. X.; Mirza, A. H.; Pickering, B. F.; Jaffrey, S. R. Alternative splicing of *METTL3* explains apparently METTL3-independent m^{6}A modifications in mRNA. *PLoS Biol.* **2022**, *20* (7), No. e3001683.
(32) Su, X.; Feng, Y.; Qu, Y.; Mu, D. Association between methyltransferase-like 3 and non-small cell lung cancer: pathogenesis, therapeutic resistance, and clinical applications. *Transl Lung Cancer Res.* **2024**, *13* (5), 1121−1136. Xiao, H.; Zhao, R.; Meng, W.; Liao, Y. Effects and translatomics characteristics of a small-molecule inhibitor of METTL3 against non-small cell lung cancer. *Journal of Pharmaceutical Analysis* **2023**, *13* (6), 625−639.
(33) Liang, S.; Guan, H.; Lin, X.; Li, N.; Geng, F.; Li, J. METTL3 serves an oncogenic role in human ovarian cancer cells partially via the AKT signaling pathway. *Oncol. Lett.* **2020**, *19*, 3197−3204.
(34) Guo, Y. Q.; Wang, Q.; Wang, J. G.; Gu, Y. J.; Song, P. P.; Wang, S. Y.; Qian, X. Y.; Gao, X. METTL3 modulates m^{6}A modification of CDC25B and promotes head and neck squamous cell carcinoma malignant progression. *Exp. Hematol. Oncol.* **2022**, *11*, 14−30.

https://doi.org/10.1021/acs.jmedchem.4c02225
J. Med. Chem. 2025, 68, 2981−3003

(35) Kitamura, M.; Kato, S.; Yano, M.; Tashiro, N.; Shiratake, Y.; Sando, M.; Okauchi, T. A reagent for safe and efficient diazo-transfer to primary amines: 2-azido-1,3-dimethylimidazolinium hexafluorophosphate. *Org. Biomol. Chem.* **2014**, *12*, 4397−4406.
(36) Dutheuil, G.; Fraser, G.; Sorlet, C.; Oukoloff, K.; Lenoir, F.; Korac, J. Piperidine derivatives as METTL3 inhibitors. WO 2024/153775 A1, 25 Jul 2024.

https://doi.org/10.1021/acs.jmedchem.4c02225
J. Med. Chem. 2025, 68, 2981−3003